2018-05-09

Exploring Density Incorporation in Inverse Radiotherapy Optimization

Maria De La Luz De Ornelas
University of Miami, m.deornelasc@miami.edu

UNIVERSITY OF MIAMI

EXPLORING DENSITY INCORPORATION IN INVERSE RADIOTHERAPY OPTIMIZATION

By

Maria De La Luz De Ornelas

A DISSERTATION

Submitted to the Faculty
of the University of Miami
in partial fulfillment of the requirements for
the degree of Doctor of Philosophy

Coral Gables, Florida

May 2018

UNIVERSITY OF MIAMI

A dissertation submitted in partial fulfillment of
the requirements for the degree of
Doctor of Philosophy

EXPLORING DENSITY INCORPORATION IN INVERSE RADIOTHERAPY OPTIMIZATION

Maria De La Luz De Ornelas

Approved:

_____ Ivaylo Mihaylov, Ph.D. Associate Professor of Radiation Oncology	_____ Weizhao Zhao, Ph.D. Professor of Biomedical Engineering
_____ Nelson Salas, Ph.D. Research Assistant Professor of Biomedical Engineering	_____ Edward Dauer, M.D. Research Associate Professor of Biomedical Engineering
_____ Nesrin Dogan, Ph.D. Professor of Radiation Oncology	_____ Guillermo Prado, Ph.D. Dean of the Graduate School

DE ORNELAS, MARIA DE LA LUZ (Ph.D., Biomedical Engineering)
Exploring Density Incorporation in Inverse Radiotherapy Optimization. (May 2018)

Abstract of a dissertation at the University of Miami.

Dissertation supervised by Associate Professor Ivaylo Mihaylov.
No. of pages in text. (113)

Inverse radiotherapy optimization is based on a cost function that tries to minimize the radiation dose to volumes within a patient's body. This dissertation explores the incorporation of electron/physical density information into the cost function. This can be termed dose-mass-based (DM) inverse optimization, as mass is the product of density and volume. Another approach for incorporating density in the optimization objective function is Energy-based optimization, where density is utilized to minimize energy deposition in mass (i.e. integral dose). The explorations herein included the investigation of sensitivity of mass-based inverse optimization with varying intensity modulation delivery parameters. The results of the study demonstrated that Energy optimization was significantly more sensitive than DM and dose-volume-based (DV) with respect to changes to both maximum segments per beam and minimum segment area. The second investigation considered the anatomical changes that occur to patients during radiotherapy. The dose-mass changes were compared between the planning CT and subsequent CTs, obtained mid-treatment and post-treatment. The results demonstrated that

significant changes to dose-mass only occur for the target volumes and no statistically significant changes were observed for the surrounding normal anatomical structures. Another comparison was performed among plans developed with DV, DM, and Energy. The results showed that the anatomical changes yielded comparable differences regardless of the type of optimization used. Since density information is included in DM and Energy, plans the results suggest that the volumetric changes that occur dominate the density changes within the volumes.

Under a third investigation, software tools were developed in order to calculate generalized equivalent uniform dose (gEUDs) and mass-weighted equivalent uniform dose (mgEUDs). mgEUD is mathematically more general than gEUD and in uniform-density media mgEUD transforms into gEUD. Incorporating physical density into the gEUD allows for a mass-weighted value representative of the uniform dose given to the mass rather than the volume. To further explore mgEUD patient outcome data for xerostomia of parotids and pneumonitis of lungs was used to correlate complication to mgEUD and in turn compare it to gEUD. The investigation determined that mgEUD values for the parotids did not show significant differences with respect to those of gEUD. In turn, lung mgEUD values demonstrated higher differences compared to values of gEUD. For radiation-induced pneumonitis of grade one and greater mgEUD showed lower standard deviations than those of gEUD. However, these differences did not translate into a better probability model of complication. The observed differences between

gEUD and mgEUD using the Lyman-Kutcher-Burman normal tissue complication model were in the range of 2-3% for doses greater than 10 Gy.

Incorporating density in inverse optimization plays a role in avoiding higher-density areas. This dissertation concluded that changes in inverse optimization delivery parameters indicated differences between volume-based and mass-based optimizations, but differences were not observed due to anatomical changes during radiotherapy treatment. The introduction of mgEUD demonstrated that there are differences in lungs with respect to gEUD and further investigation of normal tissue complication models may reveal a valuable correlation with treatment-related toxicity.

Acknowledgment

First, I would like to express my sincere gratitude to my advisor, Dr. Ivaylo Mihaylov, who has been extremely supportive during my PhD studies and guided me through. I would also like to thank Dr. Weizhao Zhao, for his direction and help, not only during these past five years, but since his BME 440 course many years ago. Furthermore, I would like to thank Dr. Nesrin Dogan for her invaluable instruction during my studies and career advice.

I am grateful for Dr. Edward Dauer and Dr. Nelson Salas for their time and suggestions. Also, I want to thank the Sylvester Comprehensive Cancer Center physicists, who have taught and helped me these past years; especially, Dr. Elizabeth Bossart, a mentor and friend. I wish to express my gratitude for her advice and willingness to help me.

I want to thank my father for his sacrifice for my sisters and myself; my mother for always pushing me to finish what I started; my in-laws for their perpetual support; my admirable sisters for motivating me; and my friend Deon Dick who encouraged me.

Last but foremost, I am indebted to my husband for his undying love and endless support. I am eternally grateful for my sons, who unknowingly inspire me to endure every failure.

Maria De La Luz De Ornelas

May 2018, Miami, Florida

Table of Contents

List of Figures

List of Tables

Chapter 1: Introduction

1.1 Cancer and Radiation Therapy

This year alone, 1,735,305 new cancer cases are expected to be diagnosed in the United States, from which 609,640 are expected to result in death due to the disease (Siegel et al., 2018). Cancer is the second leading cause of death in the US, exceeded only by heart disease. The two cancers examined in this dissertation, non-small cell lung cancer (NSCLC) and head-and-neck squamous cell carcinoma (HNSCC), comprise over a quarter of a million new cases per year in the United States. The most common treatments for cancer include surgery, chemotherapy, radiation therapy, or some combinations of the above. Radiation Therapy (RT) provides qualities that are of central importance: it is highly utilized, efficacious and cost-effective. RT is received by up to two-thirds of all cancer patients in the US, has been estimated to be responsible for 40% of all cancer cures yet represents only 5-10% of all cancer-related health expenditures (Barnett et al., 2009, Brown and Adler, 2015). Radiation therapy can be used to cure cancer, to prevent cancer from recurring, to stop or slow down its growth, and also to manage pain.

1.1.3 Radiation Physics

The physics of radiation is the science that studies radiation interaction with matter, including the energy absorption and redistribution (scattering) due to these interactions. Radiation is broadly classified into two main categories: non-ionizing

and ionizing radiation. Ionizing radiation is further divided into directly and indirectly ionizing. Directly ionizing radiation is pertinent to charged particles such as electrons, protons, alpha particles, and heavy ions. Their interaction with matter is direct, producing ionizations by collisions. The energy of the incident particle is lost along its track through the medium. If the incident particle is not energetic enough to eject an electron, it can be excited by raising electrons to higher energy levels. Uncharged particles such as x-rays, gamma rays, and neutrons are indirectly ionizing radiation. When they interact with matter they liberate directly ionizing particles.

Electromagnetic radiation consists of electromagnetic waves that propagate with their magnetic and electric fields perpendicular to each other. High frequency electromagnetic radiation is ionizing as it is capable of interacting with matter. Electromagnetic radiation traverse through media as a wave, but interacts with media as particle (photon). Photons interact stochastically undergoing a few, one, or no interactions as they pass through matter. Photons are indirectly ionizing, as they interact with the atoms in the medium they produce high-speed electrons by three major processes: photoelectric effect, Compton effect, and pair production. Depending on the interaction, secondary electrons may travel a distance before interacting. In external beam therapy using megavoltage beams, the dominant contribution to the absorbed dose is due to primary photons, which interact with electrons set in motion by Compton interactions.

Regardless of the primary source of radiation, charged particles are the ones that cause the biological effect (i.e. cell killing). As the charged particles lose energy through their track, they deposit dose, which is the mean energy imparted by ionizing radiation in matter. A precise knowledge of the spatial distribution of the absorbed dose is crucial to radiotherapy treatment planning and delivery. This spatial distribution can only be obtained if the transport of the energy by the charged particles can be modeled. Dose calculation models will be discussed in section 1.2.4.

1.1.4 Radiobiology

Radiobiology is defined as the branch of biology that studies the effects of ionizing radiation on organisms and the application in biology of radiological techniques. The exposure of biological tissues to ionizing radiation leads to ionization and excitation of their atoms. The molecules where these atoms reside tend to fall apart, resulting in free radicals. Since water is the most prevalent molecule within cells, most free radicals are produced by the radiolysis of water. Free radicals are highly unstable and readily react with other nearby molecules transferring chemical damage to them. All components of the cell will be damaged, but damage to most of them will not impact on the cell's viability. There is one cellular component that is unique and is the key to radiation damage: DNA. DNA is a double-helix molecule consisting of repeating sequence of bases, and every chromosome has approximately 200 million bases. The information needed for

protein instruction and cellular function lies in these base groups. Radiation damage to DNA may lead to the loss or modification of some genes and subsequently loss of specific functions. Enzymes within the cells are constantly monitoring the integrity of DNA and repairing it. A radiation dose of 1 Gy can lead to 1000 single-strand breaks and 40 double-strand breaks of the DNA in every cell nucleus (Mayles et al., 2007).

The main objective in radiation therapy is killing tumor cells while avoiding any damage to normal tissues. The spatial dose distribution is imperative, but biological effects also depend on the temporal distribution of dose. The speed of cellular recovery in normal tissues has been widely studied and the evidence has led to the clinical application of fractionation, by dividing the total dose into daily fractions to allow for DNA repair. Fractionation is based on the linear-quadratic equation 1, where E is the effect of a single radiation dose (*d*) in *n* fractions with total dose $D = nd$. The linear-quadratic equation is derived from the cell-survival relationship: $S = exp(-\alpha d - \beta d^2)$. Where S is cell survival,α is the linear component, and β is the quadratic component of cell kill. The ratio α/β differentiates the type of cell, with high values indicating early-responding cells and low values indicating late-responding. **Figure 4** illustrates the cell survival curves for early- and late-responding normal tissues.

$$E = n(\alpha d + \beta d^2) = \alpha D + \beta dD \qquad (1)$$

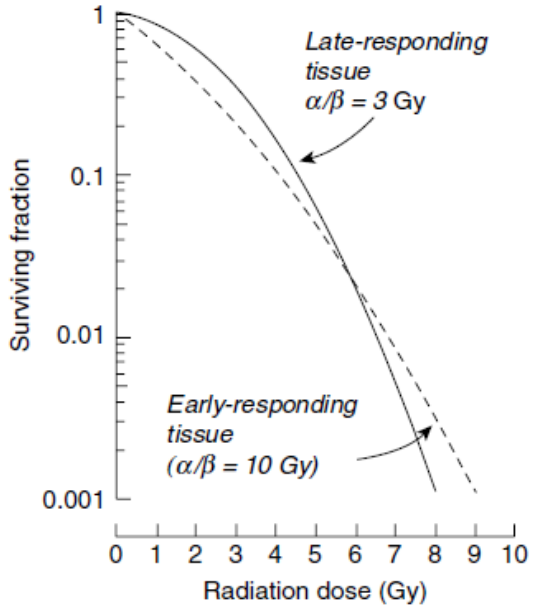

Figure 1. Cell survival curve representing early- and late-responding normal tissues. (Mayles et al., 2007)

The biological factors that influence the response of tissues to fractionated radiotherapy are popularly known as the "*5 Rs of Radiotherapy*": repair, reassortment, repopulation, reoxygenation, and radiosensitivity. Repair is derived from the fact that cellular recovery occurs within hours after exposure. Reassortment or redistribution of the cells occurs with each fraction; depending on the phase of the cell cycle when the irradiation occurred, cells will respond differently. Cells in the mitosis phase will be more sensitive to radiation than cells in the S phase. The concept of repopulation is that during 4- to 6-week treatment course, tumor cells that survive radiation may proliferate and increase the number of cells which must be killed. Also, repopulation is important for early-responding normal tissues (i.e. skin, gastrointestinal tract). Tumors that are hypoxic are more

radioresistant, therefore allowing for reoxygenation by fractionation sensitizes them. Finally, radiosensitivity of the types of cells are important for the fractionation schedule, this is true for both - normal and tumor cells.

1.1.1 Non-Small Cell Lung Cancer

Lung cancer is the second most common cancer in older men and women in the United States, with a predicted incidence for 2018 of 121,680 and 112,350, respectively. It is by far the leading cause of cancer-related deaths with only 19.5% of all patients surviving five years after diagnosis (Howlader et al., 2017). The prevalent histological types of lung cancer are non-small-cell (NSCLC) and small-cell (SCLC) lung carcinomas. NSCLCs account for approximately 80-85% of lung cancers and are divided into three main types: squamous cell, adenomarcinoma, and large-cell undifferentiated carcinoma.

The primary risk factor for lung cancer and the leading cause of cancer deaths worldwide is tobacco smoking (Alberg et al., 2013). Other factors include exposure to: secondhand tobacco smoke, occupational lung carcinogens, radiation, and indoor and outdoor air pollution. Radon is an inert gas that is odorless, tasteless, colorless, and radioactive, a direct decay from radium-226 and ultimately of uranium-238 in rocks and soil (National Cancer Institute, 2011). Radon can enter homes from the ground and collect indoors. Higher levels can be found closer to the ground (i.e. basements). Other sources can be from building materials, or from water obtained from wells that contain radon. When radon is

inhaled, it emits alpha particles in the lung causing DNA damage (Krewski et al., 2005). Another factor that has been linked to lung cancer is asbestos, which is a mineral used in building materials that breaks into small fibers that can be inhaled. Asbestos exposure has been linked to 3-4 % of lung cancers (Ettinger et al., 2014). The risk of lung cancer increases with asbestos exposure and in combination with smoking the risk is increased even further (Alberg et al., 2013).

Most lung cancers develop in the cells lining the bronchi and parts of the lung such as the bronchioles or alveoli (American Cancer Society, 2016). The lungs are two large sponge-like organs with active subunits, called alveoli (**Figure 1**). During respiration, the alveoli remove carbon dioxide from the blood and transfer oxygen from the air to the blood. As air is inhaled and exhaled, the volume of the lungs changes. The density differences due to the distribution of alveoli and the air within makes the lungs heterogeneous in density.

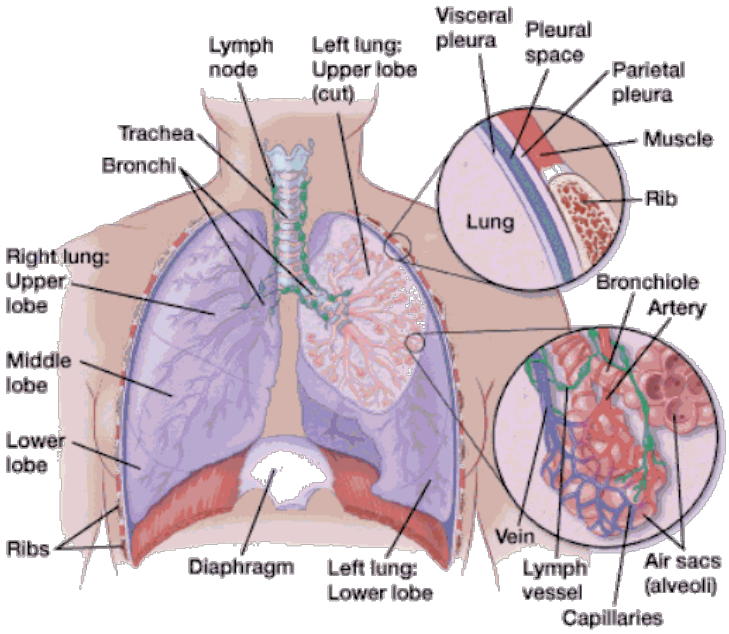

Figure 2. Lung anatomy (American Cancer Society, 2016)

Treatments for lung cancer include surgery, radiation therapy, chemotherapy, radiofrequency ablation, immunotherapy, or a combination of two or more of the aforementioned treatment options. The use of radiation for treatment includes: (1) definitive therapy for locally advanced disease, (2) definitive therapy for early-stage disease with contraindications for surgery, (3) pre- or post-operative therapy, (4) salvage therapy for limited recurrences and metastases, and/or (5) palliative therapy for incurable disease. The goal of radiotherapy is to maximize tumor control and minimize toxicity to surrounding tissues. Advanced imaging such as 4D simulation and therapy techniques such as intensity modulated (IMRT), volumetric arc (VMAT) and stereotactic body (SBRT) radiation therapies have

improved localization of dose to the tumor and reduced toxicity for the healthy organs (Ettinger et al., 2014).

Conventional 3D radiotherapy has been deemed the minimum standard. Dose escalation studies have demonstrated that doses in the order of 84 Gy lead to tumor control of 30 months or longer (Kong et al., 2005, Martel et al., 1999), yet radiation-induced toxicity limits such high levels of dose. Results from phase I RTOG 0117 demonstrated that 74 Gy in 2 Gy daily fractions using 3D radiotherapy with concurrent chemotherapy are tolerated with low rates of acute and late lung toxicities (Bradley et al., 2010). Currently, SBRT has been recommended for early-stage inoperable disease. SBRT delivers high doses per fraction (6-30 Gy), in a hypofractionated regimen of five or fewer fractions. The biologically equivalent dose (BED) for SBRT is substantially greater compared to standard fractionation treatment. A study (Ricardi et al., 2010) showed that SBRT for NSCLC patients had higher local control and survival than conventional RT.

As previously mentioned, the goal of radiation therapy is tumor control and minimization of toxicity to the surrounding healthy tissue. Dose limiting constraints have been determined for organs at risk (OARs) depending on the fractionation schedule. **Table 1** lists the OAR constraints for conventional fractionation, where V_{xx}= % of the whole OAR receiving ≥xx Gy. The total dose prescribed in a RT treatment is divided into smaller doses over a period of several days, each treatment is also referred to as a fraction. Smaller dose fractions allow healthy cell

to recuperate from the radiation damage. The dose constraints for conventionally fractionated treatments are lower than those for the hypofractionated treatments.

Table 1. Normal tissue dose-volume constraints for conventionally fractionated radiotherapy.

Organ-at-risk	Constraints in 30-35 Fractions
Spinal cord	Max ≤50 Gy
Lung	V_{20} ≤35%; V_5 ≤65%; MLD ≤20 Gy
Heart	V_{40} ≤80%; V_{45} ≤60%; V_{60} ≤30%; Mean ≤35 Gy
Esophagus	Mean ≤34 Gy; Max ≤105% of prescription dose
Brachial plexus	Max ≤66 Gy

The most important dose-limiting organ in NSCLC radiation therapy are the actual lungs. The probability and severity of radiation induced lung injury (RILI) correlates with radiation dose, fractionation schedule, and amount of irradiated lung. It also may be related to type of systemic therapy, smoking status and pre-treatment pulmonary function. RILI has two stages: early and late. Early phase (radiation pneumonitis) occurs 1-6 months after therapy manifested by cough, fever and dyspnea. Late phase (radiation fibrosis) is presented 6-7 months after RT with reduced lung capacity, progressive dyspnea and possible mortality (Evans et al., 2007). Patients treated for lung cancer present radiologic evidence of injury, but only 5-35% have symptoms (Marks et al., 2000). It is well known that lung toxicity is correlated with mean lung dose (MLD) greater than 30 Gy and 30% of the lung volume receiving 20 Gy or more (V_{20}) (Rodrigues et al., 2004, Graham et al., 1999, Kong et al., 2006).

The relationship between 3D dose distribution and pneumonitis incidence is essential to ensure minimal normal tissue toxicity and maximize tumor control

(Seppenwoolde et al., 2003). Part of designing the best radiotherapy plan is to avoid highly functioning areas. Functional imagining modalities such as functional magnetic resonance imaging (fMRI), positron emission tomography (PET) and single photon emission computed tomography (SPECT) can all be directly linked to local function (Nioutsikou et al., 2005a, Ma et al., 2008, Evans et al., 2007, Bates et al., 2009, De Jaeger et al., 2003). The main function of the lungs is the exchange of gases with the blood, and its capability can be tested with a pulmonary function tests (PTFs) testing the lung volume, capacity, rates of flow, and gas exchange. There have been various studies that have tried to establish a relation between RILI and lung function, but results have been non-definitive and any dosimetric improvement have shown to be marginal for a small subset of patients (Nioutsikou et al., 2005a, Evans et al., 2007).

1.1.2 Head-and-Neck Squamous Cell Carcinoma

The group of cancers that begin in the squamous cells that line the mucosal surfaces inside the head and neck are collectively called head-and-neck cancers (National Cancer Institute, 2017). The anatomy of the head and neck is shown in **Figure 2**, where the different regions of this type of cancer occur. HNSCC is a common form of cancer, constituting about 4% of all cancers in the United States (Howlader et al., 2017). Most of the cases are presented in people between 40 and 50 years of age, with a 3:1 ratio between men and women (Sanderson and Ironside, 2002). The most important risks associated with HN cancer are smoking

tobacco and drinking alcohol. Other risks include: chewing betel nut, consumption of certain preserved or salted foods, Epstein-Barr virus infection, radiation exposure and occupational exposure (National Cancer Institute, 2017).

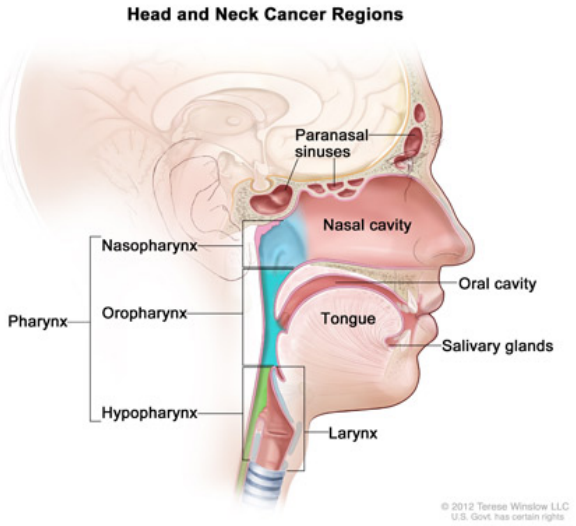

Figure 3. Head and neck cancer regions. (National Cancer Institute, 2017).

Patients with HNSCC present a challenging group, where the successful management of the disease requires a high degree of expertise and careful assessment of risk levels. The therapeutic approach is driven by the clinical and histopathological features of the disease, host-related factors and the expected impact of the patient's quality of life (Bernier, 2009). In western countries, two-thirds of the HNSCC patients present with locally advanced disease. They are offered multidisciplinary therapies combining surgery, radiotherapy and chemotherapy (Bernier, 2009).

The current radiation therapy modalities used for HNSCC include 3D-conventional (3DCRT), IMRT, SBRT and charged particle radiation therapy. IMRT has improved the dose sparing of surrounding organs in comparison to 3DCRT (Lee et al., 2007). The standard dose prescription for nonsurgical therapy is 70 Gy to the primary disease for seven weeks (Sher et al., 2017). Hyperfractionation (reduced dose per fraction) and accelerated fractionation (multiple fractions administered per day) has been widely studied to enhance the therapeutic ratio by improving tumor control without increasing late toxicity (Bernier and Bentzen, 2003). Also, advances in technology have led to better tumor tracking during treatment such as image-guided radiation therapy, which is a technique that compliments IMRT. SBRT has been used more effectively in small tumors and usually for patients who have already undergone multiple therapeutic interventions (Owen et al., 2015).

Despite the clinical progress that has occurred in the field, loco-regional control for locally advanced HN tumors after 3 years remains between 50-60%, and 20% of the patients with stage III-IV disease will experience distant progression. Achievement of local control comes with the price of increased acute and late toxicity, such as mucositis, xerostomia, dysphagia, and skin toxicity. Xerostomia and dysphagia are the most important acute and late complications after radiotherapy that reduce quality of life (Wang and Eisbruch, 2016). Xerostomia or dry mouth is the most common complication that results from damage to the salivary glands. **Figure 3** illustrates the anatomy and location of the

salivary glands. The parotid glands located on either side of the mouth are major salivary glands producing 60-65% of saliva. The parotids have been determined to be the major factor for the severity of xerostomia, therefore their preservation has been widely studied and taken into account during radiation therapy planning. The mean dose to the parotids that reduces xerostomia and preserves part of the salivary function is less than 26-30 Gy (Wang and Eisbruch, 2016). **Table 2** lists the other OAR constraints taken into account during treatment planning.

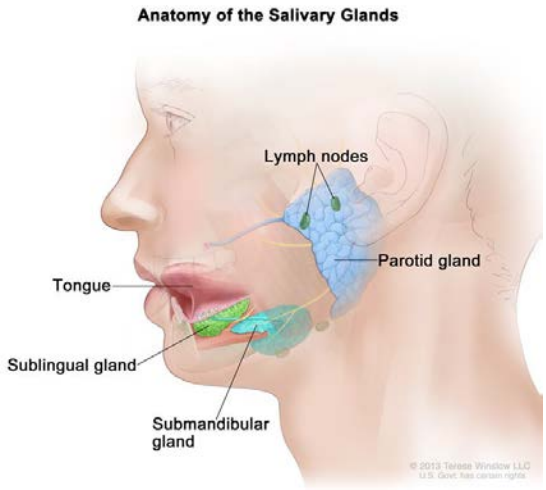

Figure 4. Anatomy of the salivary glands (National Cancer Institute, 2017).

Table 2. Head-and-Neck organs-at-risk constraints

Organ-at-risk	Constraints for 2 Gy per fraction
Braistem	Max ≤ 54 Gy
Optic Nerves	Max ≤ 50 Gy
Optic chiasm	Max ≤ 54 Gy
Spinal cord	Max ≤ 45 Gy
Parotids	Mean ≤ 26 Gy
Oral cavity	For non-oral cavity cancers ≤ 30 Gy For oral cavity cancers ≤ 50 Gy
Mandible	Max ≤ 66 Gy
Larynx	Mean ≤ 45 Gy

1.2 External Beam Radiation Therapy

Treatment devices used for radiation production are kilovoltage x-ray units, megavoltage linear accelerators, or cobalt-60 machines. Kilovoltage x-ray units were historically the first to be used for radiotherapy and they played an important role in the early development of radiotherapy, but their use has diminished after 1950 with the widespread availability of high energy photons and electrons from linear accelerators. Their use still persists for some treatments such as contact therapy (10-60 kV), superficial therapy (50-150 kV) and orthovoltage therapy (150-400 kV). Cobalt-60 machines were first used for patient treatment in Canada in 1951. Co-60 source is manufactured by irradiating Co-59 with neutrons in a nuclear reactor. The source decays to the stable isotope Ni-60 with the emission of β particles with a maximum energy of 0.32 MeV. The activated nickel nucleus

emits two γ-rays with energies of 1.17 MeV and 1.33 MeV, which constitute the useful treatment beam.

This dissertation focuses on treatments delivered with megavoltage linear accelerator machines. A linear accelerator is a device that uses high-frequency electromagnetic waves to accelerate charged particles (i.e. electrons) to high energies through a linear accelerator. The electron beam can be used to treat superficial tumors or it can be used to produce x-rays. X-rays are produced by high-energy electrons colliding with a tungsten target, from which the photons are produced through bremsstrahlung.

The main components of a linear accelerator are illustrated in **Figure 5a**. The electrons are produced by thermionic emission in the electron gun and subsequently are directed into the waveguide. The RF power generator can be a klystron or magnetron, which provides pulsed microwaves to the accelerator waveguide for electron acceleration. The accelerator waveguide consists of a high vacuum copper tube with its interior divided into discs or diaphragms. The oscillating electromagnetic field produced by the microwave generator transfers energy to the electrons within the waveguide, accelerating them in groups called electron bunches. Once the electrons have been accelerated to the desired velocity/energy, the electron beam is bent towards the treatment head with an angle of 90 ^{o} or 270^{o}, depending on the design.

The electron beam, as it exists the accelerating tube, is narrow with a width of about 3 mm. If the electron beam is used directly to treat, then a scattering foil

spreads the beam to get a uniform fluence across the treatment field. For x-ray treatment, the electron beam is directed to the target in order to produce x-rays by bremsstrahlung. The x-ray beam is collimated by a fixed primary collimator and then made uniform with a flattening filter. Other components of the treatment head are an ion chamber and a secondary collimator and are shown in **Figure 5b** and **Figure 5c** for treatment with x-ray and electron beam, respectively. The ion chamber is used to monitor the dose rate, integrated dose, and field symmetry. The secondary collimator is movable and defines the field size. There are also tertiary collimators called multileaf collimators (MLCs) that further shape the beam. The shaped beam is directed to a point called the isocenter, which is a central point around which different linac components (couch, gantry, collimators) rotate.

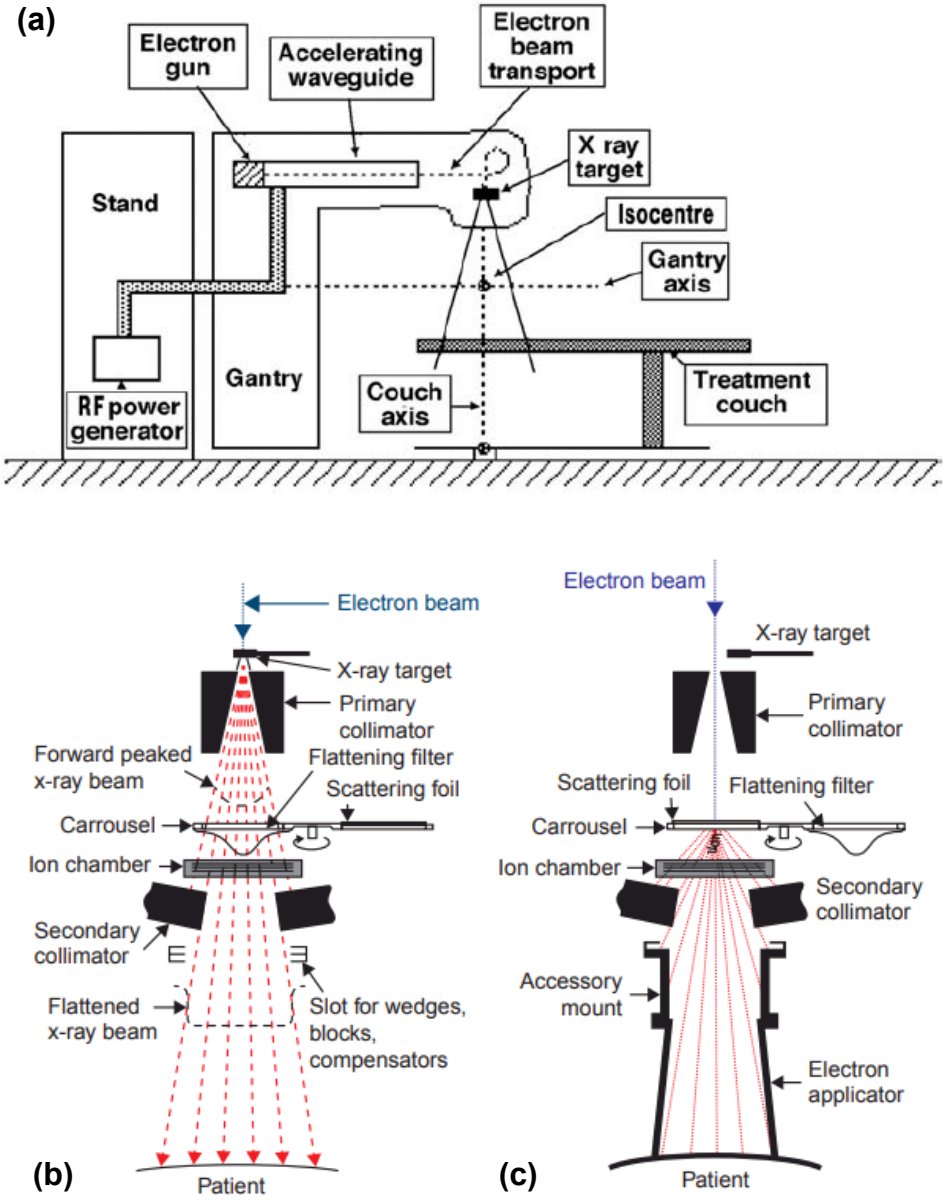

Figure 5. (a) Simple schematic of linac components. (International Atomic Energy Agency; Podgorsak, 2005). (b) Treatment head components for electron beam treatment. (c) Treatment head components for x-ray beam treatment. (Khan, 2014)

1.2.1 Three-Dimensional Conformal Radiation Therapy

Advances in radiation therapy have been ongoing since the discovery of x-rays in 1895 by Wilhelm Conrad Roentgen. At the very beginning the primary property which affected the use of x-rays was their energy, since it determined their penetration depth in human tissue. Soon after the therapeutic application of x-rays, the minimization of dose to normal tissue became important. In order to minimize and prevent damaging effects of radiation, linear accelerators were built with collimator jaws providing rectangular fields. In addition to the conventional collimator jaws, lead blocks or individually made Cerrobend cut-outs can be attached to the treatment head for beam shaping. Three-dimensional conformal radiation therapy (3DCRT), developed in the early 1990s, coincided with the widespread use of computers, which was a great advance due to the increased computational power. 3DCRT allowed tumor targeting from multiple angles, while at the same time sparing healthy tissue by shaping the beam and improving tumor control. One of the most recent innovations, the multileaf collimator (MLC), was conceptually developed in the 1980s, and widely clinically used fifteen years later (**Figure 6**). The MLC is composed of several (80 to 120) individual computer controlled tungsten “leaves” that move independently in and out of the beam for “shaping” x-ray intensity. MLCs are advantageous over blocks as they are more efficient and universal (Arthur Boyer, 2001).

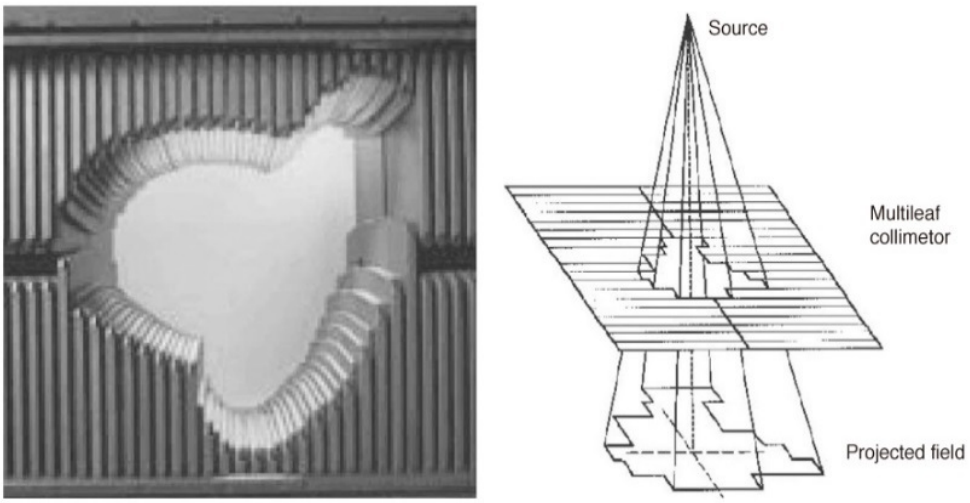

Figure 6. Multileaf collimator (MLC)

The treatment planning process for 3DCRT starts with the acquisition of anatomical information from images. Different imaging modalities can be used to localize the tumor and surrounding organs, but computed tomography (CT) is the imaging modality used for dose calculation, which will be discussed in section 1.2.2. The process by which the targets and other structures are delimitated is called segmentation. After segmentation is done, the fields and beam arrangements are designed. The ability to determine the best arrangement of the fields is enhanced by the ability to visualize by the beam's eye view (BEV), which is the display of the segmented VOIs in a plane perpendicular to the central axis of the beam.

During 3DCRT planning, the number of fields, beam directions, beam weights, and modifiers are defined by the planner. The beam modifiers are wedges, blocks, compensators, and dynamic MLCs, which help shape the desired

fluences and obtain the desired dose distribution (**Figure 7**). This type of planning, where the parameters are defined and iteratively modified manually is called forward planning. Forward panning can be labor-intensive for complex cases involving many trial-and-error iterations. The time required to plan a 3DCRT treatment depends on the experience of the planner, the speed of the planning system and the complexity of the plan. The final plan depends on numerous factors such as quality of the images, segmentation, field apertures, dose computation, plan evaluation and optimization.

All the steps mentioned for 3DCRT can be visualized as a chain of processes, illustrated in **Figure 8**. The first and second links are the requirement of a high-quality three-dimensional image and the localization of the disease and the surrounding tissue. The third and fourth links require adequate choice of the treatment parameters. The fifth, sixth and seventh links are part of the treatment planning system where the dose is computed and evaluated. The last link, patient positioning, is crucial for the correct delivery of the planned treatment. The eight individual links need to be strong and reliable in order for the patient treatment to be successful.

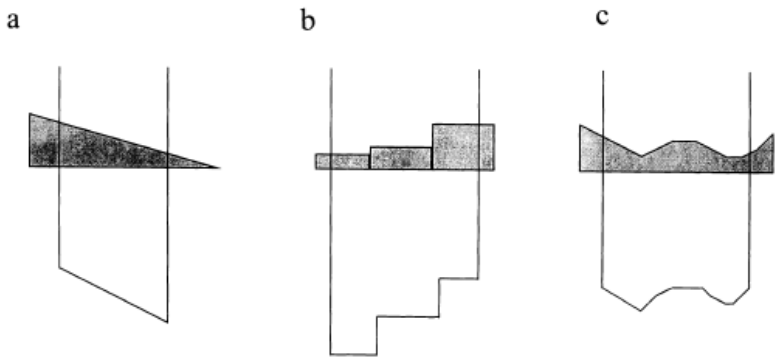

Figure 7. (a) Wedge, (b) partial transmission block, and (c) compensator. (Nutting et al., 2000).

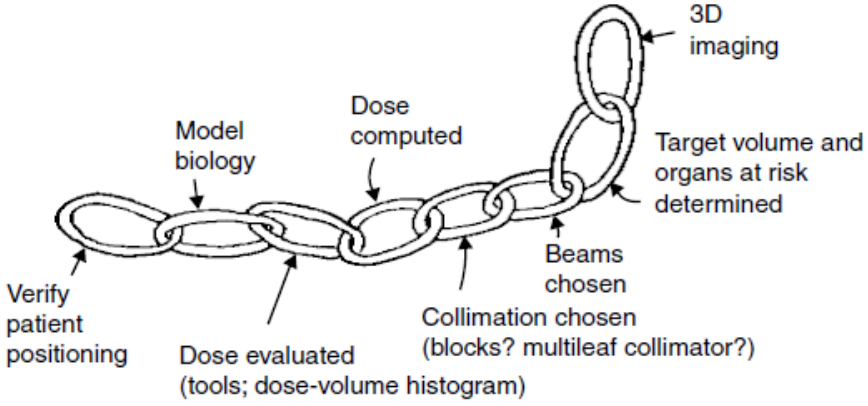

Figure 8. The chain of processes needed for the delivery of 3DCRT. (Mayles et al., 2007)

1.2.2 Computed Tomography (CT)

As mentioned in section 1.2.1, images are required to accurately delineate the volumes of interest (VOIs) for treatment planning. Modern imaging modalities for treatment planning include CT, magnetic resonance imaging, ultrasound, single photon emission tomography, and positron emission tomography. All imaging

modalities offer unique advantages in radiation therapy, but the most important is CT as it is used in dose calculation.

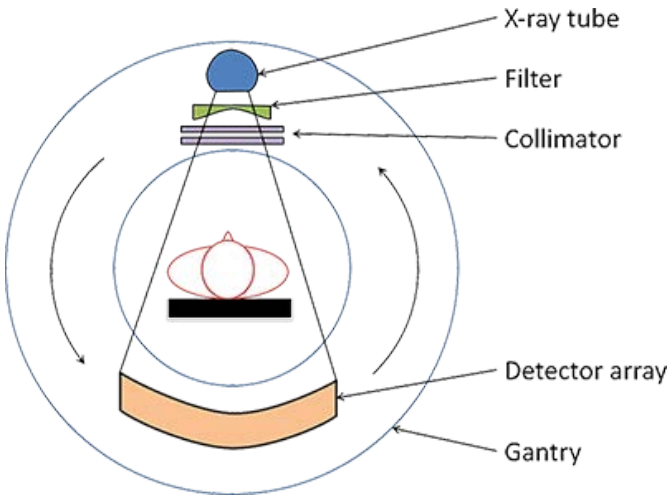

Figure 9. Computed tomography scanner schematic (Abdulla, 2018).

A CT image is a collection of transmission measurements obtained from the scanner's detectors, which are opposite to a rotating x-ray beam (**Figure 9**). The transmission measurements collected over the different orientations of the x-ray source/detectors determine the distribution of attenuation coefficients across the patient. A CT image is obtained from reconstructing a matrix of relative linear attenuation coefficients. The normalization of the tissue linear attenuation coefficients to the linear attenuation coefficient of water is known as the Hounsfield unit (HU) or CT number. The CT numbers range from -1,000 for air to +1,000 for bone and the conversion to HU is mathematically shown in equation 2, where μ is the linear attenuation coefficient.

$$HU = \frac{\mu_{tissue} - \mu_{water}}{\mu_{water}} \times 1{,}000 \qquad (2)$$

The CT numbers can be correlated to electron or physical density (electrons/cm^3), which is illustrated in **Figure 10**. In clinical practice, the CT numbers and electron density correlations for various tissues can be established by scanning a phantom (a water-like plastic), which contains areas (inserts) of different known densities that correspond to tissues such as bone, lung, and muscle.

As previously mentioned, an important feature of 3DCRT is the ability to reconstruct the patient anatomical images in planes other than the original transverse image. For 3D reconstruction, high resolution, high contrast, and thin slice thicknesses CT images are needed. In addition to high image quality, the images from simulation CT scans need to mimic the geometry of the therapy machine. Therefore, there are a few considerations to be taken into account for a CT simulator, these include: (1) a flat tabletop with the same material as the treatment couch; (2) a large diameter aperture (i.e. ≥70cm) to accommodate patient positions for radiation therapy techniques; (3) use of immobilization devices used during therapy; (4) use of external landmarks for positioning; and (5) accurate image scale in X and Y directions.

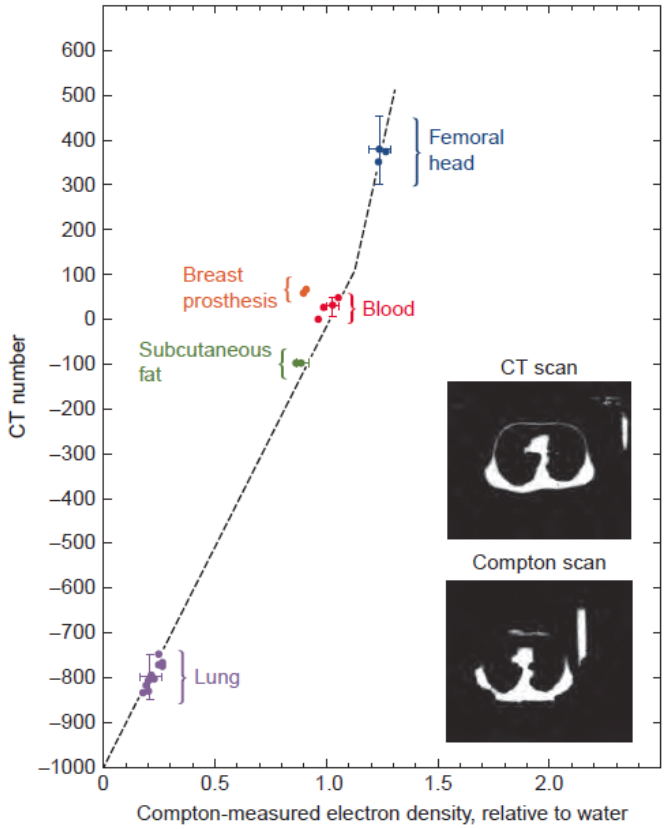

Figure 10. Computed tomography (CT) numbers as a measure of electron density relative to water (Khan, 2014)

1.2.3 Intensity Modulated Radiation Therapy (IMRT)

The idea of intensity modulated radiation therapy (IMRT) was first proposed by Brahme et al. (1982) and developed in the late 1990s as a refined method of 3DCRT by allowing beam intensity modulation. Higher intensity modulation allows for improved dose allocation of the target and better sparing of the healthy surrounding tissue. The IMRT technique is achieved by varying the radiation fluence across the beam. The fluence variation can be achieved manually with

wedges, partial transmission blocks and compensators (c.f. Figure 7). Dynamic MLCs allow for modulation of the beam, by creating subfields or segments with the moving leaves, and the desired intensity pattern is obtained from the fractional weighted summation of the individual segments (Ezzell et al., 2003). For example, combining several modulated beams achieves a conformal concave distribution around the target, which in turn avoids the surrounding normal tissue (**Figure 11**).

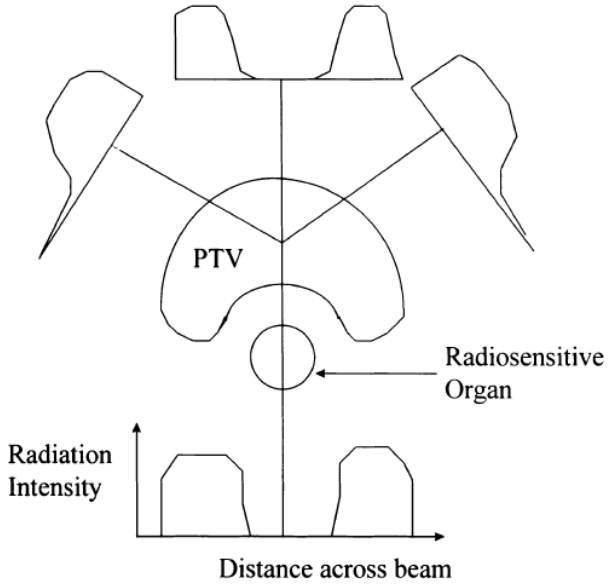

Figure 11. Dose distribution to treat a concave PTV with three beams with varying intensities. (Nutting et al., 2000)

In IMRT planning the user specifies beam directions, dose goals and/or constraints to the VOIs, and then an optimization algorithm calculates intensity patterns creating the dose distribution (Ezzell et al., 2003, Wu and Mohan, 2000). This type of optimization is called inverse optimization, meaning that the desired

results are specified by the user, and the solution is obtained afterwards through numerical algorithms. Since IMRT divides each beam direction into approximately 10^2-10^3 beamlets to be “modulated” (i.e fluence-adjusted), the solution to such large number of variables can only be achieved through inverse optimization (Ahnesjö et al., 2006).

There are two categorical methods in which inverse planning can be divided: analytic and iterative. The analytic method is a reverse reconstruction algorithm where the desired dose distribution is obtained using mathematical techniques. Assuming the dose distribution results from convolutions of point-dose kernels and kernel density, the kernel density can be obtained by deconvolving a dose kernel from the desired dose distribution. The other method is iterative, by which the beam weights are adjusted iteratively to minimize a cost function, which represents the deviation from the desired goal. Chapter 2 will expand on the details of iterative inverse planning optimization.

The implementation of IMRT not only involves the computational treatment planning system, but also the delivery system. In order to deliver the pre-calculated intensity-modulated fluence profiles, the accelerator must be equipped with a system that can deliver them. In order to deliver the intensity modulated fluence profiles, computer-controlled dynamic MLCs are the most practical and commonly used. There are three methods by which IMRT can be delivered with MLCs: fixed gantry angles, helical tomotherapy, and volumetric arc therapy (VMAT). Fixed gantry angle IMRT delivery is further divided into “step-and-shoot” and “dynamic”.

Step-and-shoot IMRT is also called segmental MLC delivery, in which the multiple fields used are divided into subfields (segments) to create the desired intensity modulation (Bortfeld et al., 1994). An example of a one-dimensional intensity profile is shown in **Figure 12a**, which can be achieved in 10 subfields by two techniques: “close-in” (**Figure 12b**) and “leaf-sweep” (**Figure 12c**). The close-in technique is defined by its name, where the segment openings reduce in size, and in the leaf-sweep technique, the leaves move from one end to the other to match the desired intensity. In the step-and-shoot method, the beam is turned off between segments, which is the difference with the dynamic MLC delivery. In the dynamic MLC delivery method, also called sliding window method, the leaves sweep simultaneously and unidirectionally, each with different velocity as a function of time while the beam is constantly on. **Figure 13** illustrates the dynamic MLC intensity profile achieved by a pair of leaves with velocities $V_A(x)$ and $V_B(x)$.

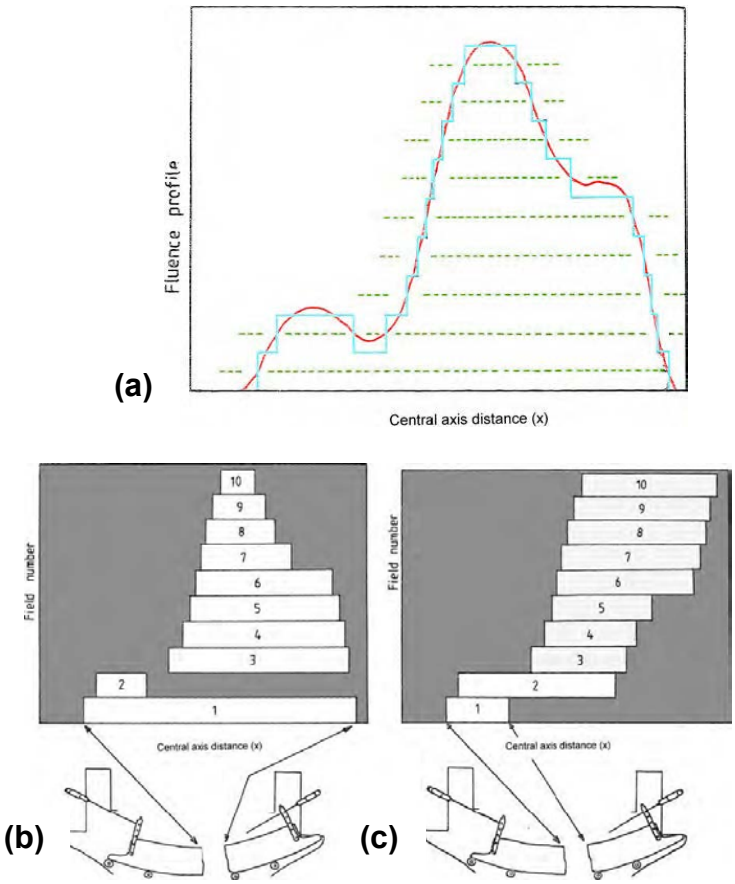

Figure 12. (a) One-dimensional fluence profile with respect to the distance from the central axis. The step-and-shoot IMRT delivery can be achieved by two techniques: (b) "close-in" and (c) "leaf-sweep". (Khan, 2014)

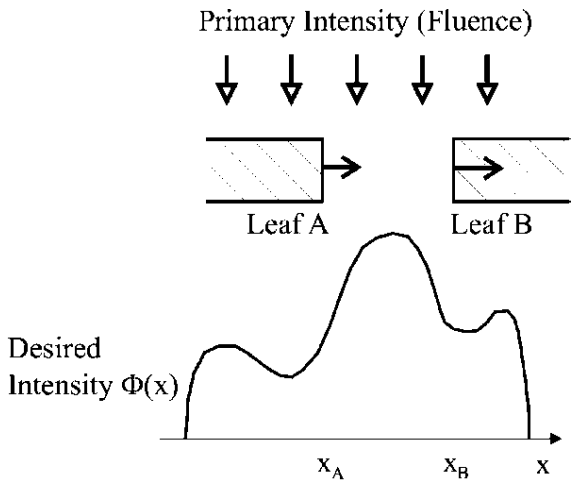

Figure 13. Dynamic MLC intensity profile. The pair of leaves with leading leaf B moving with velocity $V_B(x)$ and trailing leaf A with velocity $V_A(x)$. (Bortfeld, 2006)

1.2.4 Dose Calculation Algorithms

Radiation dose is defined as the total amount of radiation energy absorbed per unit mass. Dose is calculated by the amount of energy deposited in the media at any point where the radiation particles interact with it. The more physical processes are accounted for, and the faster the computation is, the better the dose calculation algorithm is (Lu, 2013).

Since the mid-1950s, the computerized dose calculation algorithms have been evolving. These can be divided into three broad categories: correction-based, model-based, and direct Monte Carlo. The evolution of photon dose calculation algorithms is illustrated in terms of accuracy and time in **Figure 14**. Any of the mentioned methods can be used for 3D treatment planning, but nowadays model-based and Monte Carlo are prevalent. These models are superior because of their ability to simulate radiation transport in three dimensions and more accurately

predict dose distribution under heterogeneous tissue interfaces and low-density media.

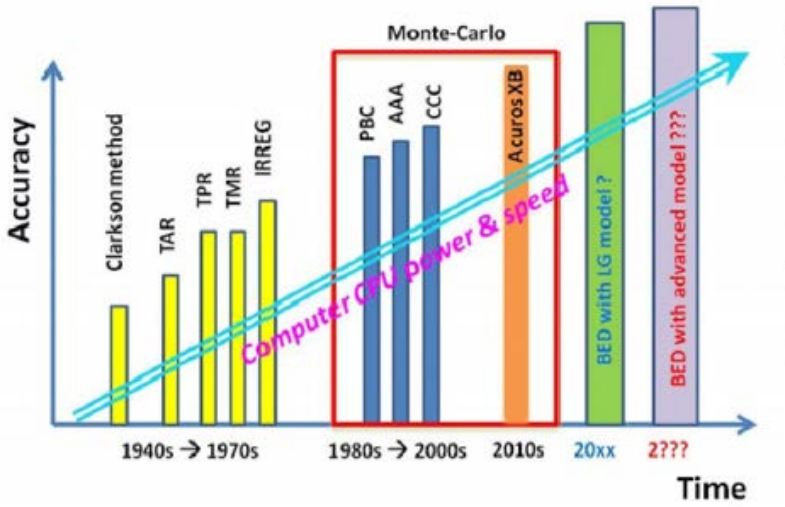

Figure 14. Evolution of photon dose calculation algorithms. (Lu, 2013)

Correction-based algorithm is an empirical dose calculation that interpolates or extrapolates dose from basic measurements in water. This algorithm works well with homogeneous media, but the accuracy with heterogeneous media such as the human body is lacking, as it cannot account for the lateral scattering when the beam transports in media. Model-based algorithms are based on physical models that simulate the actual radiation transport. Due to their ability to model primary photon energy fluence incident on a point and the distribution of energy subsequent to primary photon interaction, these models are able to simulate the transport of scattered photons and electrons away from the interaction site. The physical processes are simplified by using a convolution of the primary photon energy fluence with a kernel that describes the contribution from

scattering photons and electrons. The convolution-superposition method uses the radiological pathlength to describe inhomogeneity in media. This concept was adapted in different commercial treatment planning systems with different approaches: the pencil beam convolution (PBC), the analytical anisotropic algorithm (AAA), and collapsed cone convolution (CCC) algorithms. The difference between these is the accuracy by which the dose calculation on heterogeneous media is calculated (Lu, 2013).

The Monte Carlo technique consists of a computer program that simulates the transport of millions of photons and particles through matter. It uses physics laws to determine the probability distribution of individual interactions of photons and particles. The larger the number of simulated particles, the greater the accuracy of predicting their distributions, but with the caveat of very long computational time. The dose distribution is calculated by accruing ionizing events in voxels that give rise to energy deposition in the medium. In order to adequately predict the dose, the simulation of about a billion histories is needed. The history of a particle is defined by its path from generation until interaction; during its track the particle changes direction, loses energy, and can produce secondary particles. More recently, Acuros XB, an algorithm similar to Monte Carlo, uses the Boltzman transport equation to describe all the physical processes involved in dose deposition. These equations are solved using numerical methods, which are much faster than Monte Carlo with comparable accuracy. As suggested by Lu (2013), the next step in radiation therapy should include biological information of tissue to

primarily avoid healthy tissues and kill cancer cells directly. The investigation performed in this dissertation is in line with this idea by determining how including CT density information may improve inverse planning optimization.

Chapter 2: Dose Optimization

2.1 Dose-Volume Histogram

The most commonly used quantitative result of three dimensional (3D) dose distributions is the dose volume histogram (DVH) (Drzymala et al., 1991). The DVH may be represented in two forms: the cumulative DVH and the differential DVH. The differential DVH is formed for the volume of interest (VOI) by counting the number of voxels receiving a certain dose and this is performed over the dose range observed for the VOI. The integration of the differential DVH results in the so called cumulative DVH, which is one of the most often used tools in modern radiation therapy. **Figure 15** shows an example of an IMRT lung treatment plan with its corresponding differential DVHs, cumulative DVHs, and isodose lines. DVHs are used to analyze and compare plans in conjunction with isodose distributions displayed on the images used for dosimetric planning. Isodose lines show regions of uniform dose, high dose, or low dose, and each region's anatomic location and extent (Drzymala et al., 1991). Cumulative DVHs show the extent of dose variation within a given structure. In addition, points on DVHs (also often termed dose indices) of a VOI, are used for inverse planning in IMRT. These dose indices (DIs) used for inverse planning are usually linked to normal tissue toxicity, which is the dose limit of an organ before indicating damage.

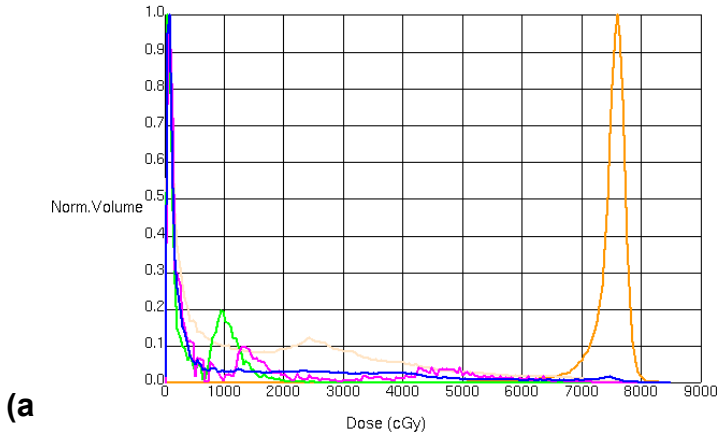

(a)

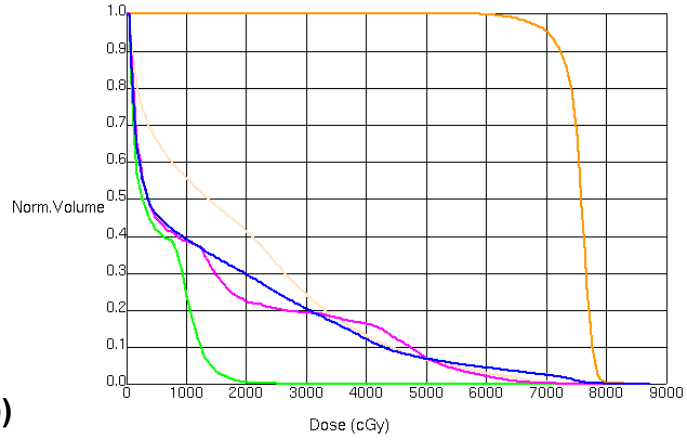

(b)

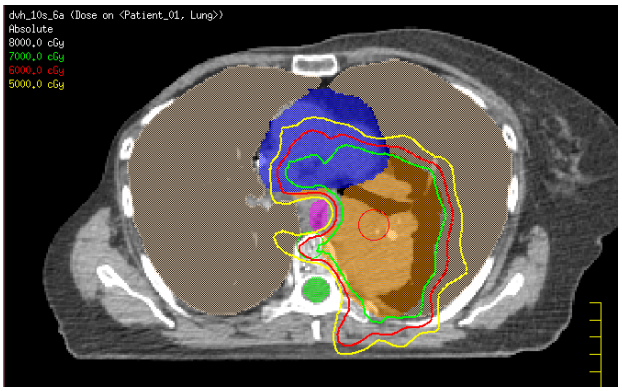

(c)

Figure 15. Example of IMRT plan of lung patient. (a) Differential DVH, (b) cumulative DVH, and dose distribution on a CT axial slice. The "PTVln" is the treated target volume, the organs at risk included: cord (green), both lungs (tan), esophagus (magenta) and heart (blue). The isodose lines represent the doses of 80, 70, 60 and 50 Gy with corresponding colors of white, green, red and yellow.

2.2 Inverse Planning Mathematics

In forward planning optimization, when the number of beams is small, the 3D dose distribution can be defined by equation 3. In this equation *D* is the 3D dose distribution, *M* is a matrix containing all the information linking beam-space to dose-space and there are *i* beams. In forward planning an acceptable solution D is achieved by trial-and-error process where beam weights w_j are adjusted

$$D=Mw_i \qquad (3)$$

Conversely in inverse optimization, the algorithm explores a range of options for w_i, such that 2D intensity maps of variable intensities are created. The optimization algorithm deduces the delivered *D* and accepts or rejects the solutions, based on predefined objectives. **Figure 16** illustrates the calculation workflow in treatment planning. For 3DCRT forward planning the process starts by defining the collimator shape by using Cerrobend cut-outs or shaping the MLCs, as seen in the upper left of the figure, and ends with the calculated dose. The plan can then be manually adjusted by repeating the settings until desired. In IMRT inverse planning process starts by defining the objective (lower left of the figure). Then, guided by the objective, the planning process is automated through an optimization feedback look (upward-directed arrows). According to the gradient of the objective with respect to the dose, these are used to find new fluence pattern directly (left-directed middle arrow). Another approach is called direct machine

parameter optimization (DMPO), where the gradients are expressed in terms of the leaf positions and segment weights (upper look of hatched arrows).

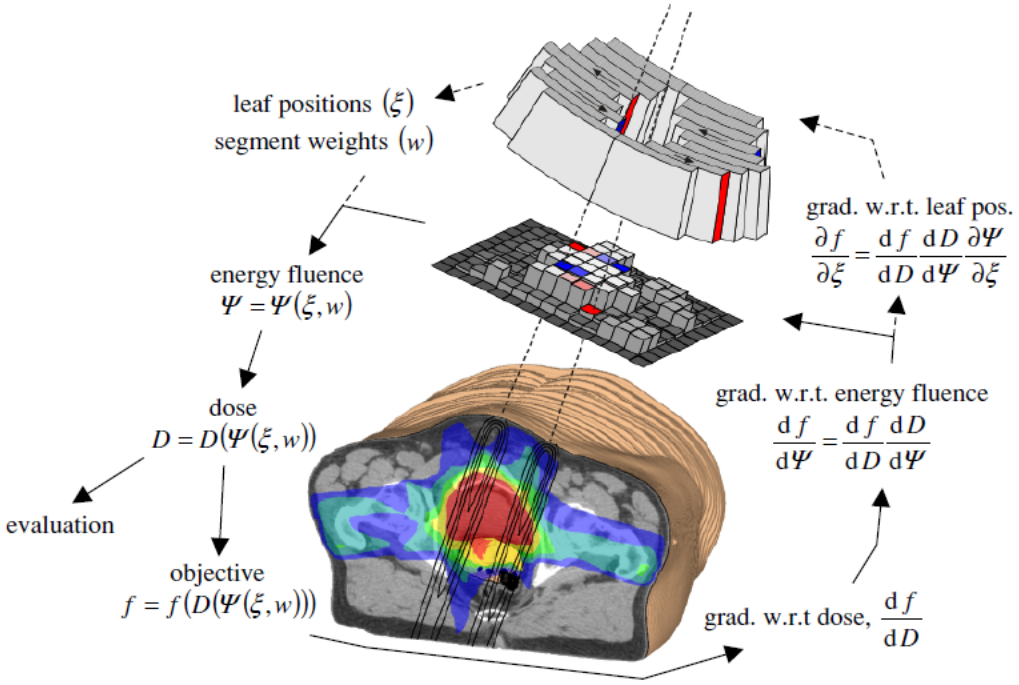

Figure 16. Treatment planning calculation workflow.

On the subject of the objective function, it is defined in equation 4 as F^k, where for maximum dose $f(d_i, d^k) = H(d_i - d^k)$ for and $f(d_i, d^k) = H(d^k - d_i)$ for minimum dose; H is the Heaviside step function, $H(x) = \int_{-\infty}^{x} \delta(t)dt$. The volume of the VOI for which F^k is evaluated is V, d_i is the dose in voxel i, and d^k is the desired dose in each voxel. The voxel's volume is v_i, and Δv_i is the voxel volume relative to the entire VOI volume ($\Delta vi = v_i / V_{total}$). The weighting factor w^k, is a dimensionless number that allows the planner to assign importance to certain objective/organ of interest. The weighting factor allows the planner to give

preference to certain objectives over others. The composite objective function, is mathematically defined in equation 5 as the sum of individual functions F^k, where τ is the set of parameters to optimize and n is the number of objectives. As this objective cost function is based on voxel volumes, it will be called DV-based (dose-volume) optimization.

$$F^k = w^k \sum_{i \in V} f(d_i, d^k) \left(\frac{d_i - d^k}{d^k}\right)^2 \Delta v_i \qquad (4)$$

$$F(\tau) = \sum_{k=1}^{n} F^k \qquad (5)$$

The DV optimization uses maximum and minimum DV functions in order to achieve desired doses on the DVH. For minimum and maximum DV objectives, the VOI volume is divided into low V_L and high V_H dose sub-volumes, which are determined by the fraction of the volume to receive the most or least dose accordingly. Evaluating equation 5 for minimum and maximum DV, V is substituted by V_L or V_H. Optimization consists of solving for the minimum $F(\tau)$, where $\tau \geq 0$. The quadratic term in equation 5 makes the function always positive, calling for the minimum difference between the desired dose and dose the voxel. In order to scale all functions uniformly for all VOI to contribute equally to the global objective function (equation 4), F^k is normalized with respect to dose by dividing by d^k and with respect to volume with the term $\Delta v_i = v_i / v_{total}$..

2.3 Dose-Mass-Based Optimization

Dose-mass histogram (DMH) employs tissue mass rather than volume as in DVH. By including tissue density information, Equation 4 can be modified to obtain dose-mass-based optimization function (equation 6). The term Δm_i is the voxel mass normalized to the total VOI mass and can be expanded as shown in equation 6. It can be noted that for constant density voxels, $\rho=\rho_i=\rho_k$ the density term may be moved in front of the summation, resulting in equation 5. Therefore, dose-mass-based (DM) optimization is mathematically more general form of dose-volume-based (DV) optimization. As the density in a VOI changes, the solution of DV and DM optimization will differ, since DM includes the density variations.

$$F^k = w^k \sum_{i \in V} f\left(d_i, d^k\right) \left(\frac{d_i - d^k}{d^k}\right)^2 \Delta m_i \qquad (4)$$

$$\Delta m_i = \frac{\rho_i \times v_i}{\sum_{k \in V} \rho_k \times v_k} \qquad (5)$$

An example of such optimization was demonstrated in a simple model of a phantom with three VOIs of different densities by Mihaylov and Moros (2014) as shown in **Figure 17**. The cubes were 10 cm x 10 cm x 10 cm with densities of 0.2 (yellow), 0.8 (red), and 1.0 (green) g/cm^3 as shown. Within the unit density cube was a cylindrical target with a diameter of 3 cm and a length of 3 cm. Two beams, one anterior-posterior (AP) and one lateral (Lat), were set to have equal weights

and an aperture of 2 cm x 2 cm with a goal to deliver a dose of 500 cGy to 95% of the target volume. A total of 833 monitor units (MUs) were required to deliver the desired prescription. After DM optimization was performed, 474 MUs were delivered though the high-density region and 359 MUs through the low-density region. Such difference in MUs illustrates the higher absorption by the high-density region.

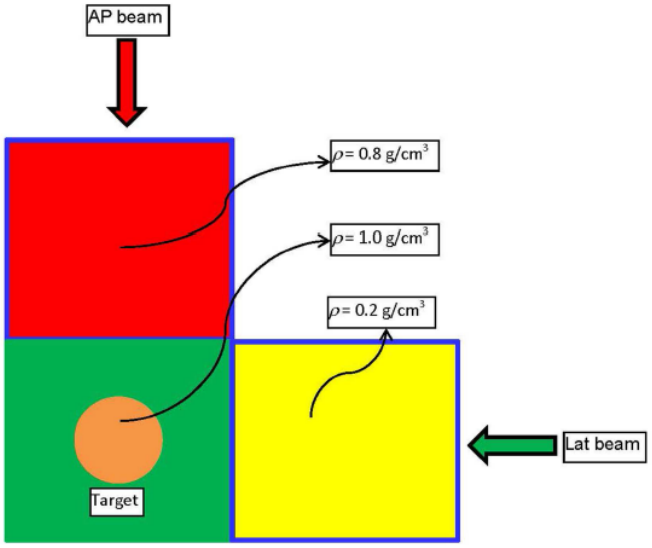

Figure 17. Model phantom with three cubes of different densities irradiated with an AP beam and a Lat beam. (Mihaylov and Moros, 2014)

Mihaylov and Moros (2014) conducted a second experiment with the same set-up to compare DV and DM optimization, the two regions of 0.8 and 0.2 densities were combined to form one OAR, to which dose was to be minimized during optimization. The target was irradiated with the two beams, AP and Lat, both centered on the target's geometric center. Each beam was only allowed to have one IMRT segment. For comparison purposes, two IMRT plans were

generated, one according to DV optimization and another with DM optimization. The inverse optimization for both were performed by decreasing the OAR dose iteratively until the standard deviation of the dose across the target reaches 6% of the prescription dose. **Figure 18** illustrates the resulting DVHs from the two optimization approaches.

The results showed that dose to the low-density region was higher for DM compared to DV optimization and the opposite is observed in the high-density region. **Table 3** lists the percent of monitor units (MUs) delivered by each beam through the corresponding high- or low-density regions. The experiment showed that taking into account density (or mass) during optimization in this simple scenario results in more dose being delivered through the low-density region (Lat beam), therefore “penalizing” more the beams passing through the high-density region (AP beam).

Table 3. Percentage of MUs delivered through each high- or low-density region. (Mihaylov and Moros, 2014)

DV		**DM**	
Low-density	*High-density*	*Low-density*	*High-density*
73.14%	26.86%	79.38%	20.62%

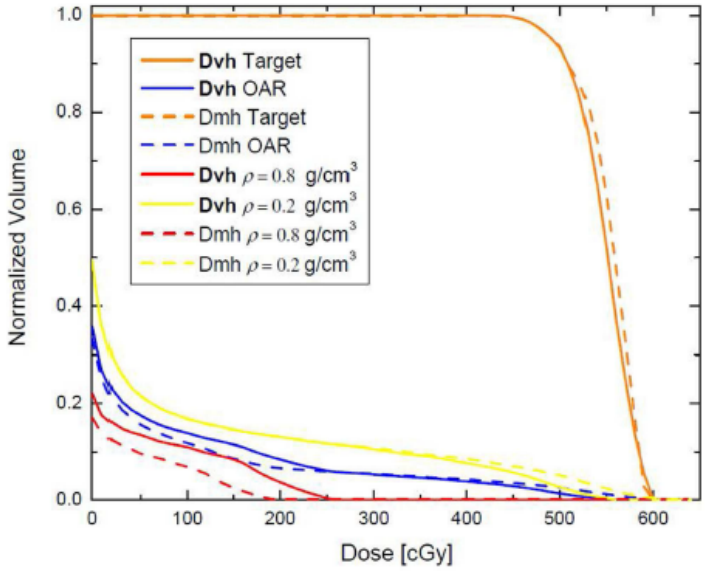

Figure 18. Resulting DVH plots from DVH-based optimization and DM optimization from plan set up shown in Figure 5. (Mihaylov and Moros, 2014)

2.3.1. Applying DM Optimization for NSCLC and HNSCC

The reasoning behind using DM optimization is that very heterogeneous media will yield a different dose distribution as density differences are accounted for. Lung density tends to be heterogeneous throughout due to blood, lung tissue and air. The proportion of the components changes continuously during respiration, changing the lung density (Verschakelen et al., 1993, Nioutsikou et al., 2005b). Since the change in electron/physical density changes the dose distribution, using DM is a more robust way of calculating dose, since the density dependency is eliminated.

A good visualization published by Nioutsikou et al. (2005b) shows the changes that occur in lung voxels during respiration and how DVH and DMH values differ. **Figure 19** illustrates two equal-volume voxels at maximum exhale (V_o) with different mass. The first voxel (VX_1) has a mass of m_o and receives a dose of 5 and the second voxel (VX_2) has a mass of $2m_o$ and receives a dose of 7. At maximum inhale, VX_1 doubles in volume and VX_2 triples in volume. The dose to VX_1 and VX_2 change to 6 and 2, respectively. The corresponding cumulative DVHs and DMH are shown in **Figure 20** for maximum exhale and maximum inhale. Volume dependency translates to breathing-phase dependency in the DVHs, whereas DMH is independent.

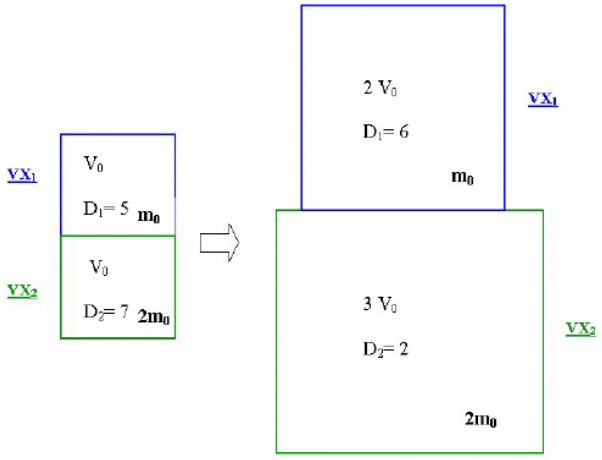

Figure 19. Two voxel representation of lung at maximum exhale (left) and maximum inhale (right). The volumes, mass and dose are displayed. (Nioutsikou et al., 2005b)

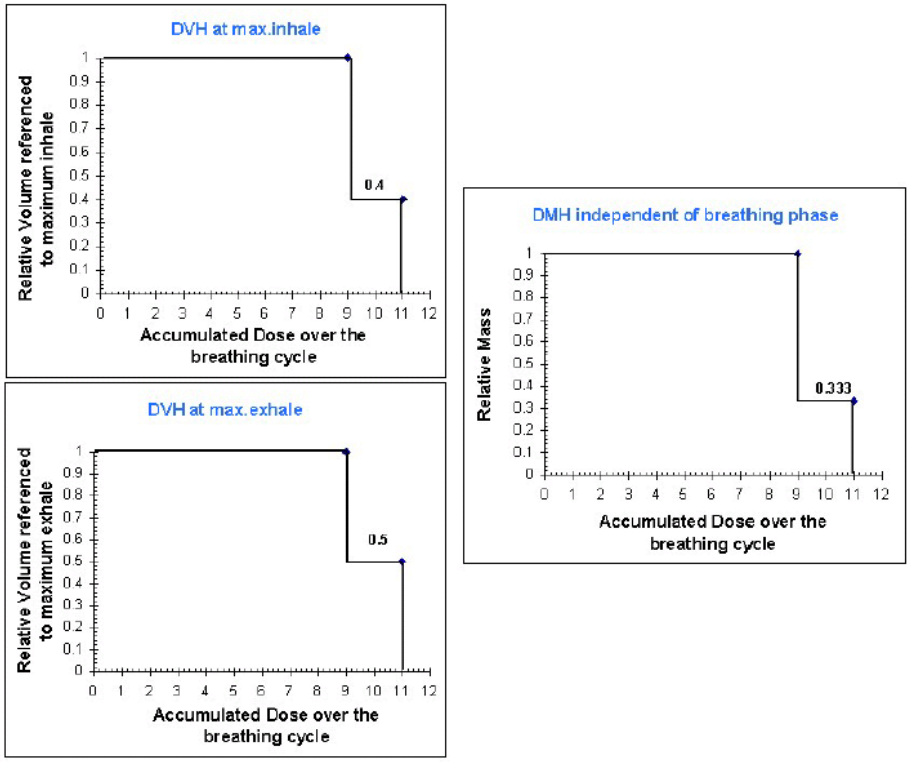

Figure 20. Dose volume histograms with volumes normalized to maximum inhale and maximum exhale. Dose mass histogram has no dependency on breathing phase. (Nioutsikou et al., 2005b)

Mihaylov and Moros (2015) demonstrated that for fourteen NSCLC patients with minimally moving thoracic lesions the majority of the dose indices taken into account for analysis, DM optimized plans resulted in lower dose to OARs compared to DV plans. In the study both DV and DM were normalized to 95% of the planning target volume (PTV) and the doses to the OARs were iteratively lowered until the standard deviation of the dose across the PTV became approximately 4% (Aaltonen et al., 1997). **Figure 21** illustrates the results of the dose indices (DIs), which are dose-volume points that are commonly used to analyze plans. The points are the DI values obtained from DM and DV plans, with

DV plans used as reference, therefore a larger normalized value means that the dose in the DM plan was lower than the DV plan. Results showed a statistically significant sparing of the OARs with DM optimization compared to DV optimization with case-by-case dependencies.

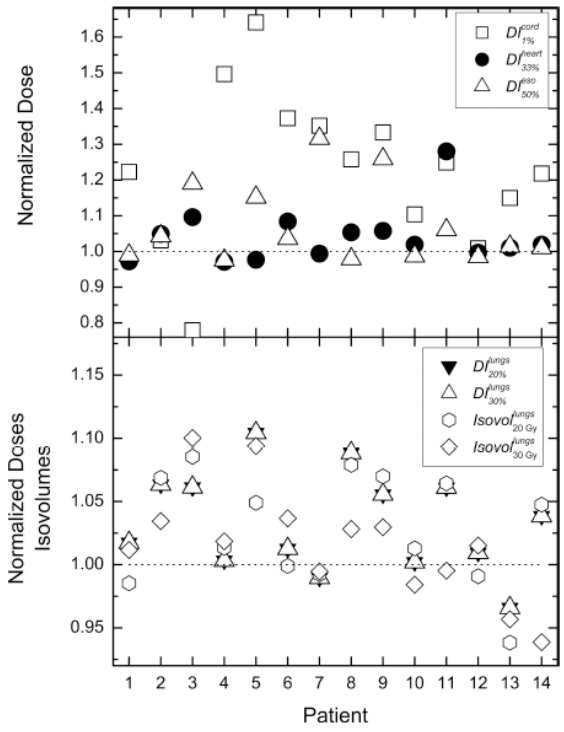

Figure 21. Normalized dose indices and isodose volumes for the fourteen patients with respect to the DM plan. The top panel illustrates the indices for heart, cord, and esophagus and the bottom panel the lung data. A value larger than one means that DM optimization resulted in lower dose. (Mihaylov and Moros, 2015)

2.4 Energy-Based Optimization

The definition of dose is energy imparted per unit mass, with units of Joules/kilogram or Gray. The amount of total imparted energy is called integral dose, $I_{,j}$, of VOI *j* composed of *x* voxels (equation 8). Since voxels are discrete, the equation can be represented in a discrete summation of all voxels within the VOI. The equation is mathematically described in equation 9. $D_{i,j}$, $m_{i,j}$, $\rho_{i,j}$, $v_{i,j}$ and $E_{i,j}$ are the dose, mass, density, volume and imparted energy of the voxel *i* in the VOI *j,* respectively. By minimizing equation 8, the total energy imparted to the VOI is minimized.

$$I_j = \int Dm\, dx \; = \int D\rho v \; dx = \int \frac{E}{\rho v} \rho v \; dx = \; \int E \; dx \qquad (8)$$

$$\mathrm{I_j} = \sum_{\mathrm{i=1}}^{\mathrm{n}} \mathrm{E_{i,j}} \qquad (9)$$

Dose calculations are based on CT derived attenuation coefficients mapped to electron density through a calibration procedure. Electron density, which scales with the physical density of the material, governs the number of Compton interactions. The electrons set in motion due to those Compton interactions, lead to ionizations, which affect the biological response in the living cells.

In order to illustrate the difference between DV and Energy optimization, Mihaylov (2014) used the same phantom set-up as in Figure 8 to compare DVH- and Energy-based optimizations. The resulting DVH plot is shown in **Figure 22**,

where the dashed and solid lines represent Energy and DV, respectively. The results showed that Energy-based plan delivered a higher maximum dose (dose to 1% of the volume) to the low-density region (564 cGy) and the combined OAR (541 cGy) compared to DV plan with 540 cGy in the low density region and 520 cGy in the OAR. On the other hand, dose to the high-density region was lower in Energy-based plan (216 cGy) versus in DVH-based plan (248 cGy). The average dose to the OAR were 45 and 50.2 cGy, respectively. Comparing the integral dose delivered the Energy plan imparted less energy for all VOIs with a value of 0.941815 J compared to DV plan with 1.09977 J. The same trend is observed with each region, as expected since the goal of Energy optimization is to reduce the energy deposition to the VOIs.

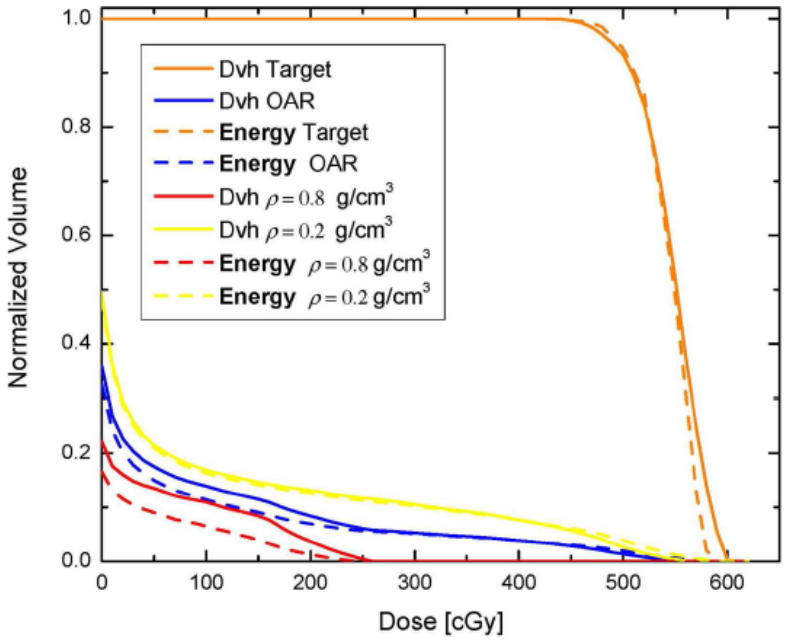

Figure 22. Resulting DVH plots from the two inverse optimization approaches: DVH-based optimization and Energy-based optimization. (Mihaylov, 2014).

2.4.1. Applying Energy-Based Optimization for NSCLC and HNSCC

As in DM optimization, the heterogeneous anatomy of NSCLC and HNSCC make the density inclusion in optimization an interesting concept to explore. Mihaylov (2016) expanded on the integral dose concept to twenty NSCLC patients by creating two IMRT plans: DV and Energy. Both plans used the same objectives and target dose were set and the optimization stopped once the standard deviation across the PTV was 4%. DIs, isovolumes and equivalent uniform dose values were used for the comparison. **Figure 23** illustrates the comparison of the two plans with normalization to the DVH values for the DIs and isovolumes for all OARs for each patient. A value larger than unity corresponds to a larger dose or volume for the Energy-based plan compared to the DV plan. The majority of the patients showed a lower dose to the surrounding organs with the Energy-based plans, but variations occurred for each patient, which may be due to the differences in anatomy, physiology and tumor location.

The same concept of integral dose can be applied to HNSCC as the surrounding anatomy is heterogeneous and complex. Ultimately, the goal is to lower the dose to the surrounding tissues for lesser side effects, which may be achieved by minimizing the energy deposited.

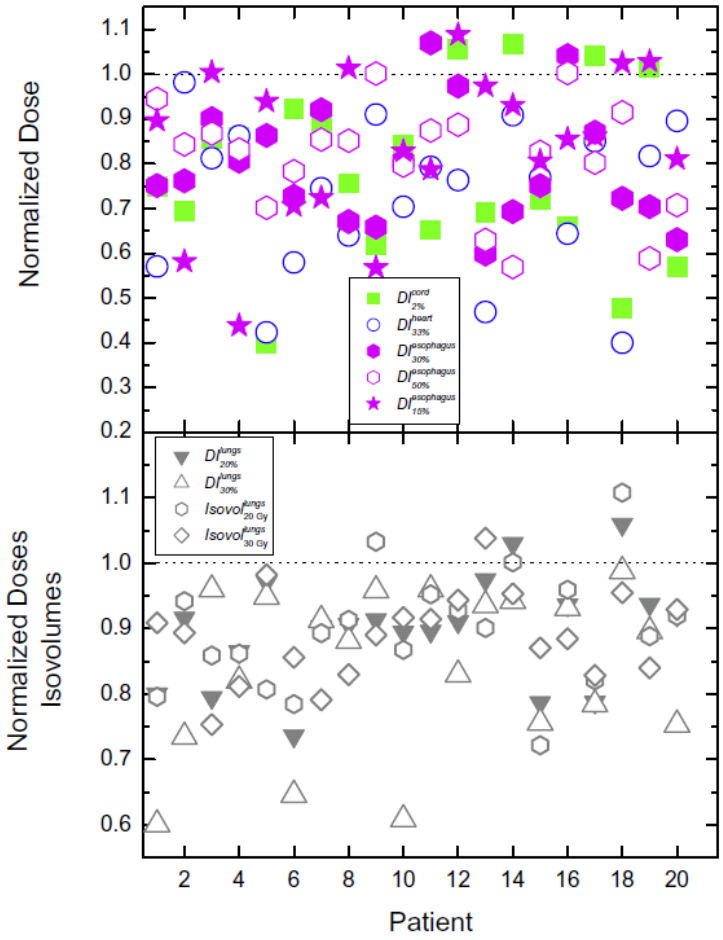

Figure 23. Normalized DIs and isovolumes for all OARs per patient. The top panel presents the DIs for spinal cord, heart and esophagus. The bottom panel presents the DIs and isovolumes for the lungs. (Mihaylov, 2016).

Chapter 3. Mass-Based Optimization Sensitivity to IMRT Optimization Parameters

Inverse optimization for IMRT planning can be performed in either one- or two-step process. In the two-step process, fluence optimization is performed first and leaf trajectories are generated afterwards (Hårdemark, 2003, Shepard et al., 2002). In the more recent one-step approach, the MLC leaf-sequencing step and other physical constraint parameters are included in the optimization in order to generate deliverable plans. One-step optimization can be performed by direct aperture optimization (DAO), which uses simulated annealing algorithm, or direct machine parameter optimization (DMPO) using gradient descent algorithm (Li et al., 2015). DMPO was illustrated in section 2.2 with Figure 16, where depending on the gradient with respect to the dose, the changes to the leaf parameters change. This type of optimization reduces the number of segments and monitor units. In addition, it improves conformity and homogeneity without compromising plan quality (Hårdemark, 2003, Dobler et al., 2009, Ludlum and Xia, 2008). Studies have demonstrated that the different IMRT parameters defined prior to optimization, such as the number of segments, segment area, number of intensity levels, number of MUs per beam and MLC leaf increment affect plan outcome (Mittauer et al., 2013, Derbyshire et al., 2009, Cheong et al., 2013, Worthy and Wu, 2009, Jiang et al., 2005)

It has been reported that large number of segments and small segment areas result in more complex plans with higher intensity modulation (Cheong et al., 2013). The mentioned study concluded that a range between 80-120 number

of segments and 4-8 cm^2 for segment area was appropriate for complex HN cases, but decreasing the number of segments and increasing segment area for more simple cases showed good plan quality. Another study (Mittauer et al., 2013) suggested that limiting the minimum segment area to less than 5 cm^2 preserves the dose to OARs and PTVs within objectives and dose deviations within 4% for HN cases. For lung cases, Nioutsikou et al. (2004) demonstrated that with a maximum of 40 segments in total with five fields the dose homogeneity would not be compromised.

Given that changes in IMRT parameters alter the optimization solutions, part of this dissertation will study the sensitivity of DM and Energy optimization modalities to IMRT parameter variations. Such investigations will lead to further understanding of density effects on plan optimization.

3.1 Study on Sensitivity to IMRT Parameter Variation

The purpose of this study was to compare DM, Energy and DV optimization sensitivity to changes in IMRT delivery parameters.

3.1.1 Methods and Materials

Twelve NSCLC and twelve HNSCC patients were retrospectively optimized using DV, DM and Energy optimization. In a preliminary study the comparison was made between DM and DV, including two patients for the NSCLC and two patients for HNSCC were used for comparison. For all optimization approaches, changes

to two parameters were studied: number of IMRT segments (5 and 10 per beam) and the minimum segment area (2 and 6 cm^2). Four plans were developed for each combination (**Table 4**) in order to determine the sensitivity of the two parameters. Optimization was performed with the treatment planning system (TPS) Pinnacle Research version V.8.1y (Philips Radiation Oncology Systems, Fitchburg, WI) with DMPO. The dose grid was 3 mm^3 for the HNSCC cases and 4 mm^3 for the NSCLC cases. The number of beams, beam angles, and minimum MUs per segment were the same for both optimizations approaches for each patient. During optimization, doses to the OARs were iteratively lowered until the standard deviation across the PTV was above between 3.0% and 5.0%, since a standard deviation of no more than 5% has been recommended to achieve proper tumor control (Aaltonen et al., 1997). For each patient DV, Energy, and DM plans were normalized such that 95% of the PTV received the same dose. Plan quality was evaluated by dose indices (DIs), which represent the dose delivered to a certain anatomical structure volume. For the NSCLC cases, DIs assessed included: 1% cord (1% of spinal cord volume), 33% heart, 20% and 30% both lungs, and 50% esophagus. In the HNSCC cases: 1% spinal cord, 1% brainstem, 50% left/right parotids, 50% larynx, and 50% esophagus. The comparisons between different plans were made relative to the parameter changes, using a paired two-tailed student's t-test. The average values of the DIs were found to be statistically significant if p value ≤ 0.05.

Table 4. Four plans developed involved the combination of 5 segments and 10 segments with areas 2 cm^2 and 6 cm^2. Each plan was named according to the combination of segments (s) and area (a): 5s_2a, 5s_10s, 10s_2a and 10s_6a.

	5 segments	**10 segments**
2 cm^2 area	*5s_2a*	*10s_2a*
6 cm^2 area	*5s_6a*	*10s_6a*

3.1.2 Results

For the preliminary study with four patients, the resulting average percent change for each DI was not significant in either optimization modality. For most cases, DM optimization seemed to be more sensitive to segment area change than DV, but such conclusion could not be reached with the small number of cases studied. Twenty more cases where included in the cohort, with which Energy-based plans showed more definitive results. The NSCLC cases resulted in larger changes observed with Energy plans compared to DM and DV plans. **Figure 24** shows the average dose for each DI evaluated or each of the three inverse optimization approaches. When increasing the segment area and keeping 5 segments/beam, the Energy plans showed statistically significant increase in dose to 1% cord, 30% both lungs and 50% esophagus. The Energy plans also results in statistically significant changes to maximum dose to cord with 10 segments/beam when increasing the segment area and also when the number of

segments increased keeping the segment area 6 cm^2. DM plans resulted in significant difference when the area increased for 50% esophagus with 10 segments/beam. The DV plans showed significant difference in 20% both lungs when the number of segments increased while keeping the segment area 6 cm^2. **Table 5** lists the p-values of the statistical tests, where $p \leq 0.05$ was considered to be statistically significant.

Another approach to illustrate the results was to use the closest arrangement of parameters clinically used and compare the results for DM and Energy. According to DV-based studies 10 segments/beam and a minimum segment area of about 5 cm^2 are appropriate for lung cases (Nioutsikou et al., 2004). **Figure 25** illustrates the average dose per DI for each parameter combination with respect to 10 segments/beam and 6 cm^2 segments area for comparison purposes due to being the closest clinically used parameters.

The HN cases showed larger changes with the Energy plans (cf. **Figure 26**), with statistically significant differences when increasing the segment area for 1% brainstem, 50% left and right parotid and 50% larynx using either number of segments per beam (5 and 10 segments/beam). Also, increasing the segment area with 10 segments/beam was on average statistically significant for cord 1%. Furthermore, increasing the number of segments using 2cm^2 segment area, resulted in significant decrease for 50% parotids and 50% esophagus. The DV plans showed statistically significant increase when increasing the number of segments (2 and 6 cm^2) for 50% larynx. In addition, esophagus 50% resulted in

significant difference when using 6cm^2 segment area and increasing the number of segments. Finally, the only DI that showed significant difference in the DM plans was 50% larynx when increasing the segment area with 10 segments/beam. **Table 6** lists the resulting statistical test p-values due to changing parameters. The same approach to illustrate and compare with clinically used parameters as for the NSCLC cases is shown in **Figure 27**. The values shown in the figure are with respect to 10 segments/beam and 2 cm^2 minimum segment area.

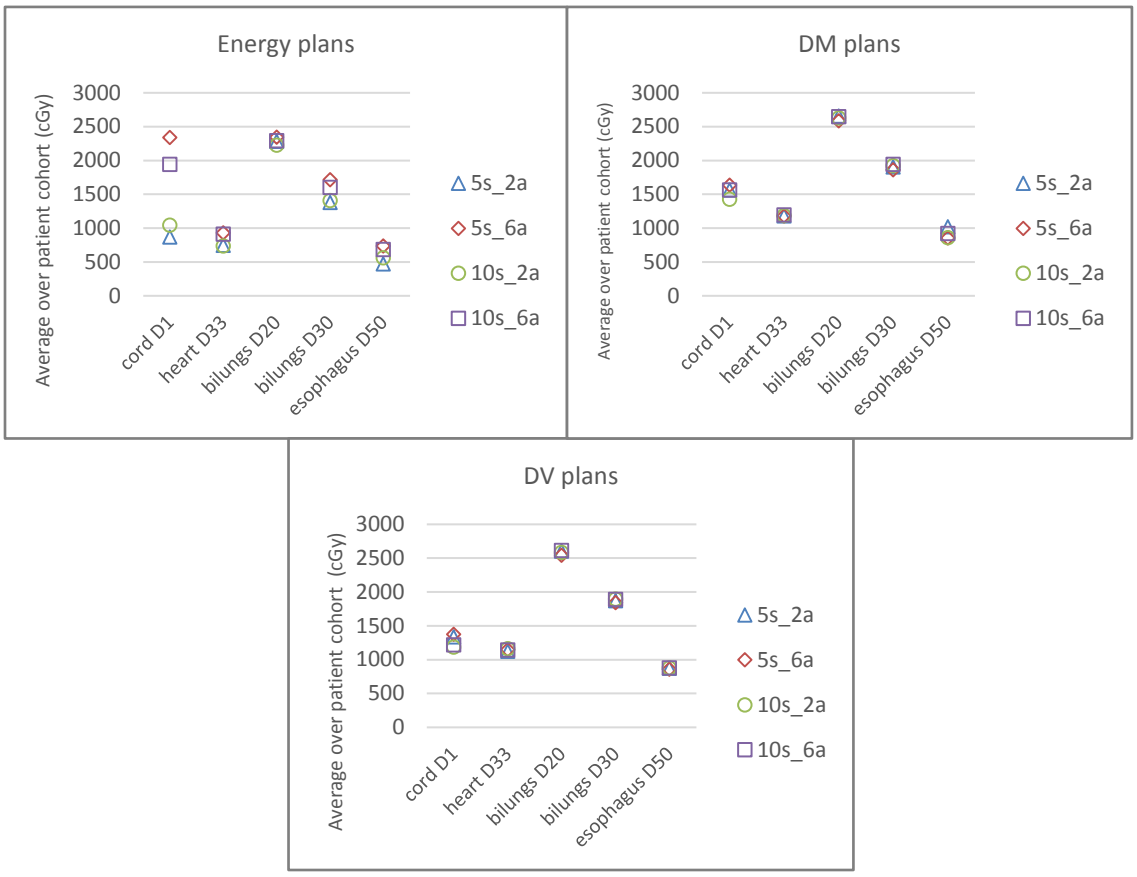

Figure 24. Lung cases: Each point represents the average dose index for the four different segment parameter combinations: 5 or 10 segments/beam and 2 or 6 cm^2 segment area. (Legend indicates arrangement - 5s_2a denotes 5 segments with minimum area of 2 cm^2)

Table 5. Lung cases: Statistical test p-values for the change in parameter (i.e. change in segment area) per optimization approach. The highlighted values represent those with statistical significance.

	changing segment area (5 segments/beam)			**changing segment area (10 segments/beam)**		
	Energy	***DM***	***DV***	***Energy***	***DM***	***DV***
cord D1	0.0001	0.6574	0.4690	0.0299	0.2944	0.0576
heart D33	0.2439	0.9820	0.5871	0.3258	0.7085	0.4397
bilungs D20	0.6051	0.0531	0.0741	0.4656	0.5939	0.2509
bilungs D30	0.0188	0.1954	0.5161	0.1491	0.5980	0.7441
esophagus D50	0.0062	0.3301	0.6213	0.3373	0.3339	0.9615
	changing number of segments/beam (2cm^2)			**changing number of segments/beam (6cm^2)**		
	Energy	***DM***	***DV***	***Energy***	***DM***	***DV***
cord D1	0.1098	0.5233	0.1283	0.0376	0.2987	0.1786
heart D33	0.8593	0.9519	0.3240	0.3979	0.3539	0.7971
bilungs D20	0.2501	0.5730	0.4727	0.2583	0.1398	0.0368
bilungs D30	0.7009	0.5716	0.4511	0.1208	0.0873	0.0969
esophagus D50	0.2845	0.3891	0.8366	0.3792	0.0191	0.4598

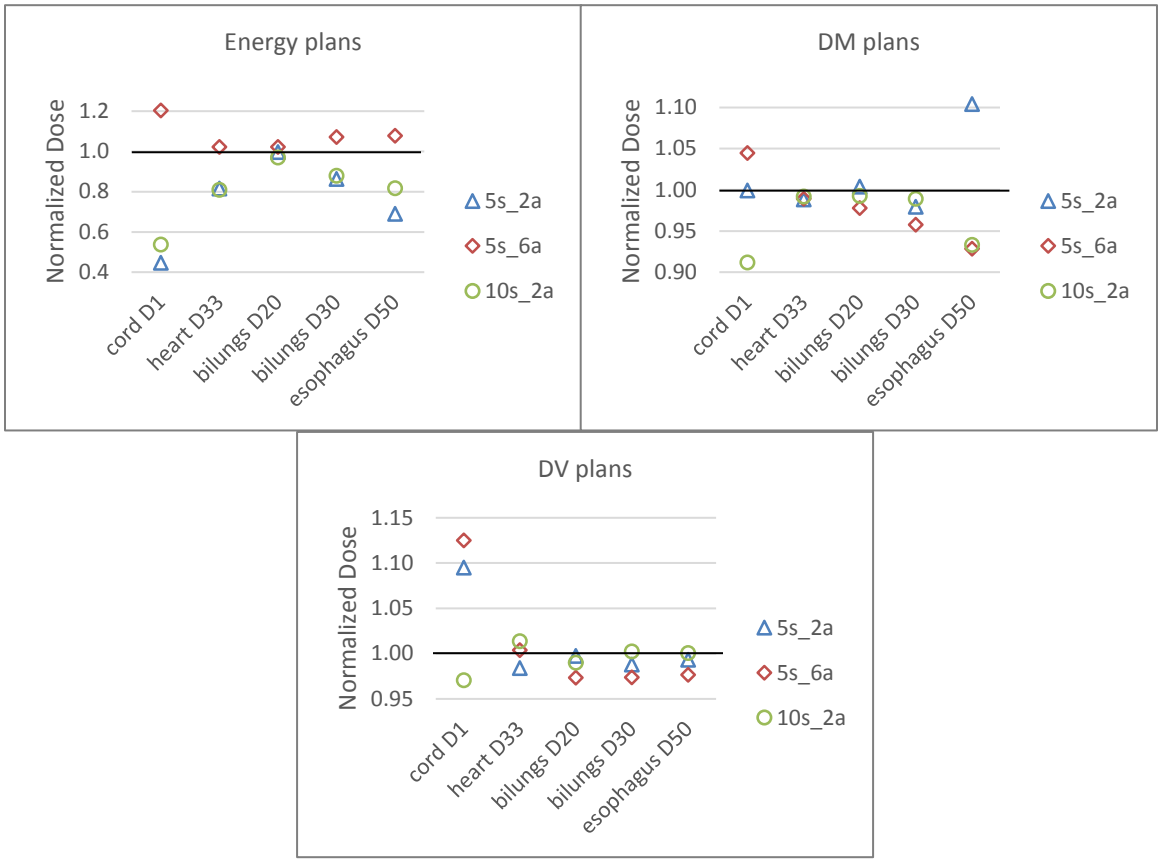

Figure 25. Lung cases: Each point represents the normalized dose of the parameter combination (i.e. 5s_6a is 5 segments/beam with 6 cm^2 area) with respect to 10 segments/beam with 6 cm^2 as it is the most closely resembling the clinically used DMPO segment parameters in DV optimization. It is important to note the differences in the ordinate scale as the Energy plans showed significantly larger variation in values with a range of [0.69-1.2]. Also, values for bilungs D20 in the Energy plans plot are close and almost cannot be differentiated. The same issue occurs for heart D33 in the DM plans plot.

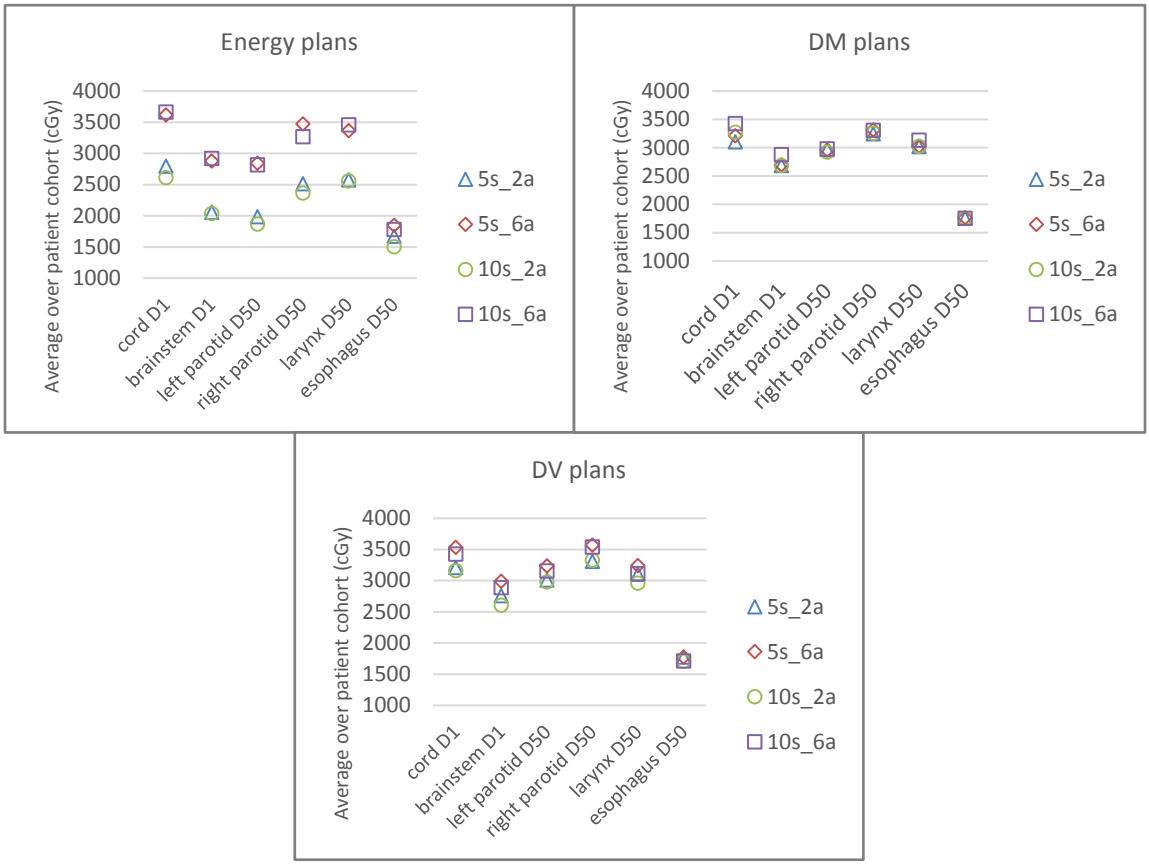

Figure 26. HN cases: Each point represents the average dose index for the four different segment parameter combinations: 5 or 10 segments/beam and 2 or 6 cm2 segment area. (Legend indicates arrangement - 5s_2a denotes 5 segments with minimum area of 2 cm2)

Table 6. HN cases: Statistical test p-values for the change in parameter (i.e. change in segment area) per optimization approach. The highlighted values represent those with statistical significance.

	changing segment area (5 segments/beam)			**changing segment area (10 segments/beam)**		
	Energy	***DM***	***DV***	***Energy***	***DM***	***DV***
cord D1	0.1005	0.4378	0.2124	0.0281	0.2164	0.2584
brainstem D1	0.0242	0.9088	0.3386	0.0132	0.1617	0.2206
left parotid D50	0.0169	0.8135	0.2709	0.0157	0.4620	0.3903
right parotid D50	0.0195	0.3329	0.1816	0.0194	0.5034	0.2780
larynx D50	0.0415	0.9682	0.3965	0.0213	0.0191	0.3404
esophagus D50	0.2200	0.7829	0.9903	0.1238	0.8440	0.7586
	changing number of segments/beam (2cm^2)			**changing number of segments/beam (6cm^2)**		
	Energy	***DM***	***DV***	***Energy***	***DM***	***DV***
cord D1	0.1063	0.2902	0.5726	0.6113	0.2736	0.1712
brainstem D1	0.7555	0.9917	0.1643	0.5608	0.3199	0.1896
left parotid D50	0.0471	0.6215	0.7128	0.7400	0.7568	0.0849
right parotid D50	0.0326	0.8966	0.8255	0.1127	0.9568	0.5292
larynx D50	0.6792	0.9853	0.0359	0.1971	0.1486	0.0254
esophagus D50	0.0180	0.9061	0.2466	0.4014	0.6116	0.0354

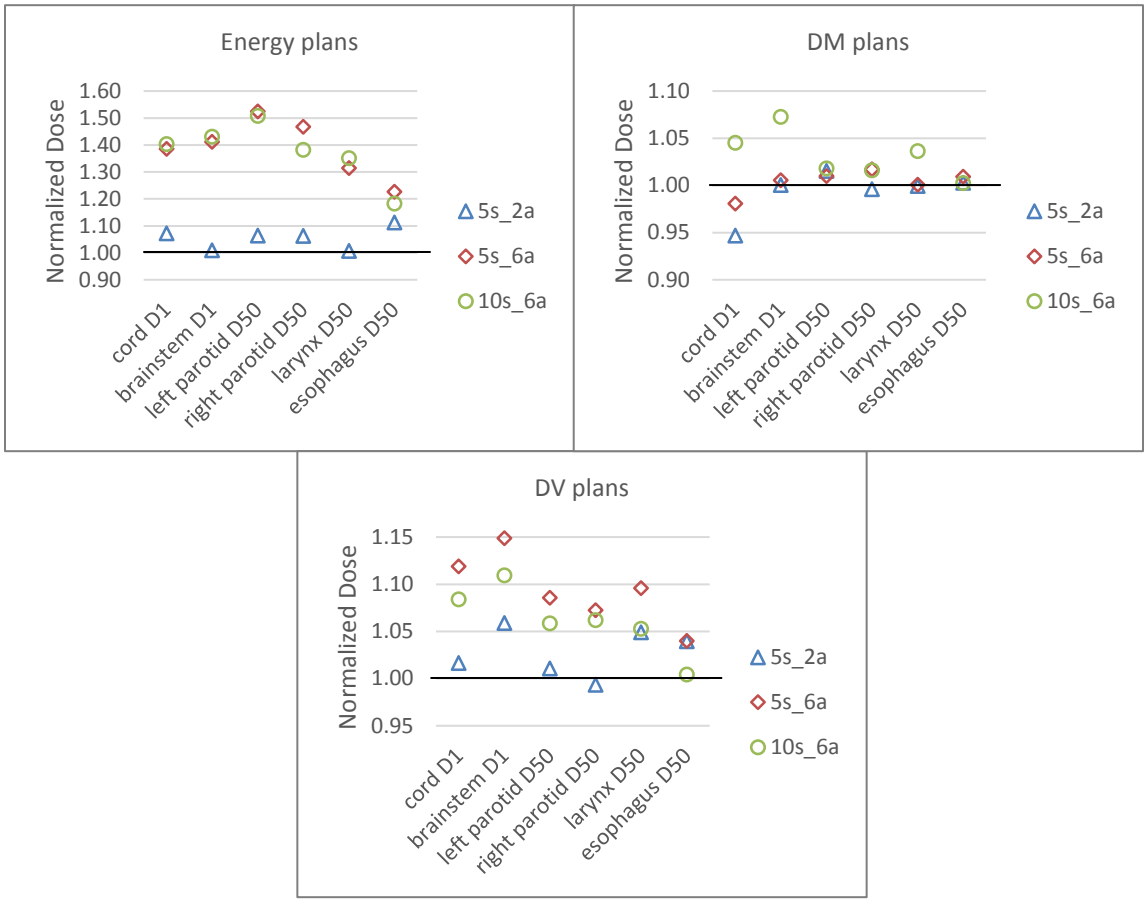

Figure 27. HN cases: Each point represents the normalized dose of the parameter combination (i.e. 5s_2a is 5 segments/beam with 2 cm^2 area) with respect to 10 segments/beam with 2 cm^2 as it is the parameters most closely resembling the clinically used DMPO segment parameters in DV optimization. It is important to note the differences in the ordinate scale as the Energy plans showed significantly larger variation in values (range: [1-1.51]) compared to DM (range: [0.95-1.07]) and DV (range: [0.99-1.15]). Some point in the DM plot cannot be differentiated since the values are very close.

3.2.3 Discussion and Conclusion on the Sensitivity to IMRT Parameter Variation

Accounting for density variations within volumes of interest affects the inverse optimization results. Dose-mass inverse optimization increases OAR

sparing for NSCLC cases, with some case dependencies (Mihaylov and Moros, 2015), while Energy-based plans (Mihaylov, 2016) result in lower dose to the surrounding OARs in NSCLC cancer, supporting the notion that explicit incorporation of density distribution in the optimization functions affects the resulting inverse optimization solutions. Mass-based inverse optimization depends on IMRT beam parameters, such as minimum segment area and number of segments per beam was investigated. In conventional DV optimization, the choice of IMRT parameters affects the plan quality. It is important to note that highly modulated plans with very small segment areas may not be deliverable due to hardware limitations (McNiven et al., 2010, Li et al., 2003). Dosimetric differences between planned and measured dose can be attributed to dose calculation errors in the treatment planning system, errors by the dosimeter used, and errors of the linac (Li et al., 2003). Errors of the linac include errors due to mechanical limitations of the MLCs, which typically occur with very complex and highly modulated plans.

In line with the mentioned DV studies, in the DM and Energy plans the segment area smaller than 5 cm^2 and number of segments greater than 80 was beneficial for HN cases for most DIs. However, the average maximum dose to the cord showed better sparing with 5 segments per beam for the DM plans. The results for the DV plans were in agreement with previously published studies, where the 10s_2a parameter combination showed the lowest average doses for all DIs and the doses increased with larger segment area and less segments per beam. Similar to those results were the results for the Energy DIs, but the changes

were larger as the segment area increased. In somewhat simpler lung anatomy, the number of segments can be smaller and the allowed segment area could be larger for clinically viable solutions. The results for improving dose sparing with a certain combination was not uniform across DIs for the DV plans, but the dose changes were small when varying the parameters. The Energy plans showed that a segment area of 2 cm^2 improved most DIs, regardless of the number of segments. The most notable improvement was observed for the maximum dose to the cord. This might be due to the relative location of the beams with respect to the target as well as the steep density gradient around the spinal cord where soft tissue is adjacent to the bones of the vertebrae. The results indicate that with the use of a single objective function, as is Energy optimization, any variation of IMRT segment parameters changes the plan to larger extent than in multi objective optimization approaches such as DV and DM. Therefore, it is important to appropriately determine the DMPO parameters for Energy optimization.

Energy-based optimization showed more sensitivity to IMRT segment parameters compared to DV and DM optimization. The sensitivity was more notable in the HNSCC cases than NSCLC cases, which may be due to the close proximity of many OARs, which is related to the higher necessary beam intensity modulation. Furthermore, the Energy plans were more sensitive to the segment area than to the number of segments per beam.

Chapter 4. Dosimetric Changes due to Changing Patient Anatomy during Radiotherapy Treatment

Anatomical changes during the course of radiotherapy treatment are not uncommon. Change in NSCLC cancer patients may include atelectasis, pleural effusion, pneumonia/pneumonitis, and tumor regression/progression (Bosmans et al., 2006, Britton et al., 2007, Erridge et al., 2003, Fox et al., 2009, Møller et al., 2014, Kwint et al., 2014). Dosimetric changes due to anatomical alterations have been analyzed and found to be significant in some cases (Britton et al., 2009, Yamada et al., 2006, Kataria et al., 2014). A study looking at anatomical change, respiratory motion, and baseline shifts during radiotherapy found that only anatomical changes resulted in large dosimetric changes compared to the other two factors (Schmidt et al., 2013). They also mentioned that the large anatomical changes that cannot be accounted for by increased margins, lead to large dosimetric changes. These kind of changes require plan adaptation.

Anatomical changes in HNSCC cases are even more pronounced than in NSCLC due to weight loss, tumor, and nodal shrinkage (Barker Jr et al., 2004, Schwartz and Dong, 2011, Barkley Jr and Fletcher, 1977). Changes in parotid volumes in HN cases include shrinkage and displacement during radiation treatment, resulting in a 10% increase of mean dose (Lee et al., 2008, O'Daniel et al., 2007, Wu et al., 2009). These and other studies have found that target coverage was not significantly changed with the use of appropriate margins (Ballivy et al., 2006). Many studies have analyzed such changes in order to

determine the necessity of adaptive radiotherapy to determine re-planning strategies (Barker Jr et al., 2004, Schwartz and Dong, 2011, Castadot et al., 2010).

As in the case of IMRT beam parameter dependencies discussed in the previous chapter, the inclusion of density in DM and Energy inverse optimization approaches may be more sensitive to changes during RT than in most commonly used DVH optimization.

4.1 Study on DMH Dependence on HNSCC Patient Anatomy

Anatomical changes not only mean volumetric changes, but also changes to mass. Since the volumetric changes have been well established in the literature, this study seeks to determine the sensitivity of DMHs.

4.1.1 Methods and Materials

Eight patients undergoing radiotherapy treatment for HNSCC were scanned during the third and sixth week of treatment. These second (CT2) and third (CT3) CTs were co-registered to the planning CT (CT1). Contours were propagated via deformable image registration from CT1 and doses were re-calculated with the original treatment plans. DMHs were extracted for each CT image set. DMH sensitivity was assessed by dose-mass indices (DMIs), which represent the dose delivered to a certain mass of and anatomical structure. DMIs included: dose to 98%, 95% and 2% of the target masses (PTV1, PTV2, and PTV3) and OARs: cord DMI2%, brainstem DMI2%, left_ and right_parotid DMI2% and DMI50%, and

mandible DMI2%. A two-tailed paired t-test was used to compare changes to DMIs in CT2 and CT3 with respect to CT1 (CT2/CT1 and CT3/CT1).

4.1.2 Results and Conclusions

Results showed a significantly lower dose to the DMI98% for the three PTVs. For all patients DMI98% to all PTVs were lower for CT2 and CT3 compared to CT1, except for one patient case which PTV3 DMI98% was 0.2 Gy higher in CT2 compared to CT1. For the three PTVs DMI95% was significantly different between CT2 and CT1 (CT2/CT1) for PTV1 and between CT3 and CT1 (CT3/CT1) for PTV3, and both (CT2/CT1 and CT3/CT1) for PTV2. Dose reduction to the PTV1 prescription (DMI95%) was in the range from 0.2 Gy to 4.9 Gy. The lower coverage to the three PTVs suggests the need to re-plan about half-way through the treatment (CT2). Maximum dose, on the other hand, was significantly higher for PTV1 and PTV2 in both CT2/CT1 and CT3/CT1, and only CT2/CT1 for PTV3.

On the contrary, doses to OARs did not show significant changes. **Figure 28** illustrates the average percent change of CT2/CT1 and CT3/CT1 for DMIs of OARs and PTVs. Maximum doses to cord and mandible were higher as RT progressed but, for brainstem DMI2% was reduced. Changes were most pronounced for the left_parotid DMI50% in CT2/CT1 with an average percent change and standard deviation of 22.58% ± 75.95. Right_parotid DMI50% had the largest change in CT3/CT1 (14.21% ± 38.21). This large change and variation was

due to patient 2, who had substantial variation between CTs compared to the other patients.

It was found that changes in anatomy significantly changed dose-mass coverage for the planning targets, making it necessary to re-plan in order to maintain the therapeutic goals. Maximum dose to the PTVs increased significantly as RT progresses, which may not be problematic as long as the high dose remains within the gross tumor volume. Doses to OARs were minimally affected and the differences were not significant.

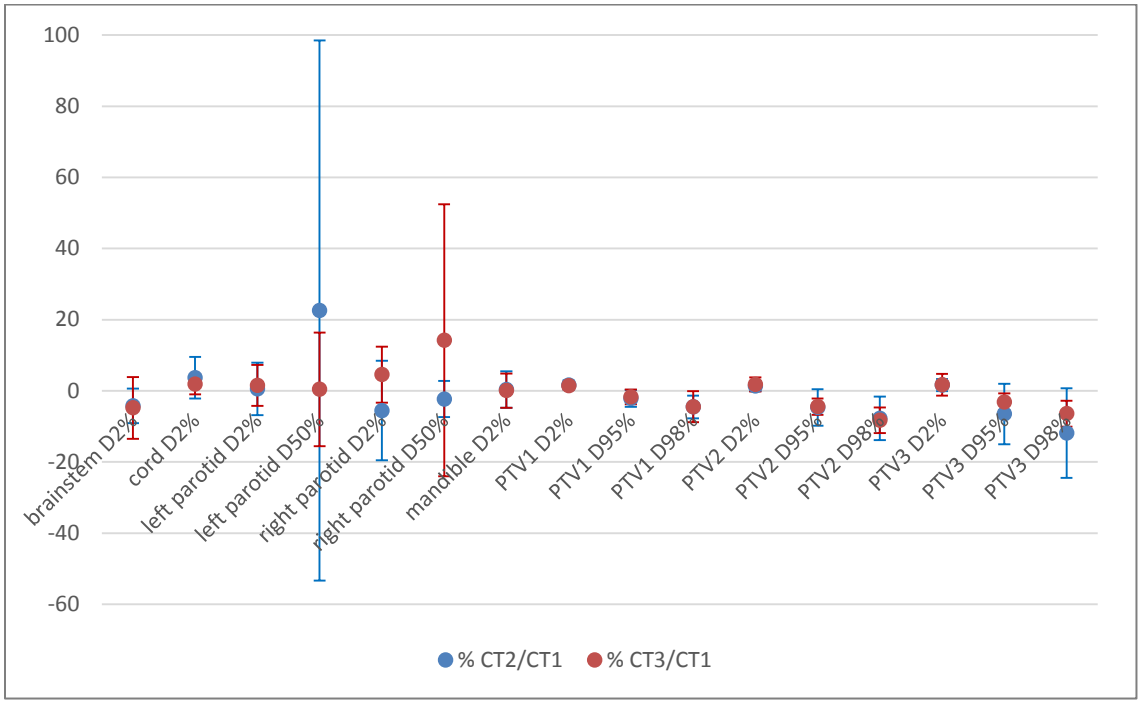

Figure 28. Average percent change between CT2 relative to CT1 (CT2/CT1) and CT3 relative to CT1 (CT3/CT1) for each DMI. Positive values correspond to increased dose for the corresponding DMI. Error bars show the standard deviation of the percent change for all patients.

4.2 Study on DM Optimization Sensitivity to Anatomical Changes

The purpose of this study was to compare the sensitivity of DM and DV optimization to anatomical changes during radiotherapy.

4.2.1 Methods and Materials

Six NSCLC and six HNSCC patients were CT scanned during radiotherapy course multiple times. The notation is as follows: CT1 is the pre-planning CT, CT2 is mid-RT, and CT3 is after completion of the radiotherapy regimen. Scans 2 and 3 were co-registered to the planning CT1 to deformably propagate the contours. Two plans were generated for each patient on CT1: DV and DM. For each case Energy and DV plans were generated on the planning CT1 using nine equispaced beams using step-and-shoot IMRT. DV plans were used as a benchmark since current clinical practice is based predominantly on this type of optimization. During optimization, doses to the organs at risk were iteratively lowered until the standard deviation across the PTV was ~4.0%. All plans were normalized to 95% of the prescription dose to the PTV: 80 Gy in 35 fractions for the NSCLC cases and 70 Gy to the primary PTV for the HN cases. Subsequently, the plans were transferred to CT2 and CT3, and doses were recalculated. This scenario represents the actual treatment regimen, where no plan adaptation is employed. DIs were used in order to compare the two plans and the changes occurring with RT progression. DIs used for the NSCLC cases were: PTV D95%, cord D2%, both lungs D20% and

D30%, and heart D33%. For the HN cases, DIs included: PTV1 D95%, cord D2%, brainstem D2%, left_ and right_parotid D2% and D50%.

4.2.2 Results and Conclusions

The absolute relative (in percent) change between the final CT (CT3) and the planning CT (CT1) yielded larger average values for DM plans compared to DV plans for most DIs, except PTV D95 for NSCLC cases and left_parotid D50 for HNSCC cases. **Table 7** lists the average changes for the NSCLC cases and **Table 8** the changes for HNSCC cases. Some DI changes between CT2 and CT1 and between CT3 and CT2 were on average larger for DM plans compared to DV plans. The observed changes are comparable between DV and DM optimization schemes.

Table 7. Average absolute value percent change between CTs for the NSCLC cases.

NSCLC cases	**CT2-CT1**		**CT3-CT1**		**CT3-CT2**	
Dose Index	**DV**	**DM**	**DV**	**DM**	**DV**	**DM**
PTV D95	2.07	2.22	6.87	4.98	5.15	3.91
Cord D2	15.10	34.35	18.71	20.21	17.39	20.78
Heart D33	29.92	33.02	26.36	37.23	15.32	16.65
Both lungs D20	11.90	11.25	16.28	17.71	10.01	9.86
Both lungs D30	11.47	11.38	15.03	16.48	10.67	9.74

Table 8. Average absolute value percent change between CTs for the HNSCC cases.

HNSCC cases	CT2-CT1		CT3-CT1		CT3-CT2	
Dose Index	**DV**	**DM**	**DV**	**DM**	**DV**	**DM**
PTV1hn D95	1.04	0.81	0.78	0.84	1.35	1.24
Cord D02	14.25	14.71	16.44	18.00	6.19	6.39
Brainstem D02	7.88	7.91	7.86	8.98	5.46	5.85
Left_parotid D02	8.27	7.07	6.06	6.31	9.82	8.40
Left_parotid D50	4.29	4.12	8.19	7.95	6.27	7.11
Right_parotid D02	6.22	6.61	29.41	30.03	25.47	26.53
Right_parotid D50	3.79	4.55	8.30	10.08	4.81	5.96

4.3 Study on Energy Optimization Sensitivity to Anatomical Changes

The purpose of this study was to compare the stability of Energy-based inverse optimization on changing anatomy in HNSCC.

4.3.1 Methods and Materials

Fifteen HNSCC patients were scanned during treatment. As with the previous study (section 4.2), the mid-treatment scan (CT2) was rigidly registered and all VOIs were deformably propagated from the planning CT (CT1). For each case Energy and DV plans were generated on the planning CT1 using nine equispaced beams using step-and-shoot IMRT. As in the previous study (section 4.2), DVH was used as the benchmark for the comparison. During optimization, doses to the organs at risk were iteratively lowered until the standard deviation

across the PTV was ~4.0%. All plans were normalized to 95% of the prescription dose to the primary PTV: 70 Gy in 33 fractions. The plans were then transferred to the subsequent CTs without any modification/re-optimization. Dose indices (DIs) were obtained for plan stability evaluation. DIs used included: PTV1 D95%, cord D2%, brainstem D2%, left_ and right_parotid D2% and Dmean, esophagus D50%, larynx Dmean and mandible D2%. Absolute percent differences between DIs from subsequent CTs were tallied. Furthermore, a two-tailed paired t-test was used to compare changes on the absolute dose differences of the DIs. In addition, the clinical plans, used for actual treatment, were also analyzed.

4.3.2 Results and Conclusions

Regardless of the optimization modality the changes that occurred were small with some exceptions. The average absolute percent change between CT1 and CT2 for each DI is listed in **Table 9**, where the values in bold represent the higher value between DV and Energy optimized plans. Change for six out of the ten DIs was larger for DV plans compared to Energy plans, but there were no statistically significant differences between the two optimization modalities for any DI when comparing the absolute doses. This result indicates that the DI differences are drawn from a distribution with mean zero and some symmetric spread around the mean. The high average absolute value percent change for the esophagus D50% was due to an outlier where the absolute doses were very low. For this case the second CT was difficult to register to the planning CT due to neck tilt and

noticeable area shrinkage, leading to higher dose to the volumes of interest. The changes observed in the clinical plans were comparable to the tested plans, with slightly smaller changes, which was large due again to one outlier. The variability of the change for the two modes of optimization is illustrated in **Figure 29**. The outlier is not shown in the figure as it had a 295% change.

Even though Energy-based inverse optimization depends explicitly (through the optimization cost function) on the density distribution within volumes, the dosimetric changes that occur during radiation treatment are small and comparable to that of DV plans for HNSCCC. With either optimization large differences may occur due to noticeable weight loss and/or positioning errors.

Table 9. Average value percent change between planning CT (CT1) and mid-treatment CT (CT2) for each optimization approach: DV and Energy. In addition the clinically used results are listed for reference purpose.

	Absolute value percent change between CT1 & CT2		
Dose Index	**DV**	**Energy**	**Clinical**
PTV D95	0.78	1.06	1.95
cord D02	13.09	10.12	3.22
brainstem D02	11.15	10.73	5.35
esophagus D50	25.26	45.68	56.55
larynx Dmean	8.23	6.89	5.07
left parotid D02	9.63	4.94	4.20
left parotid Dmean	6.14	7.87	15.16
right parotid D02	11.65	6.45	5.96
right parotid Dmean	6.08	6.32	4.93
mandible D02	5.10	4.45	3.40

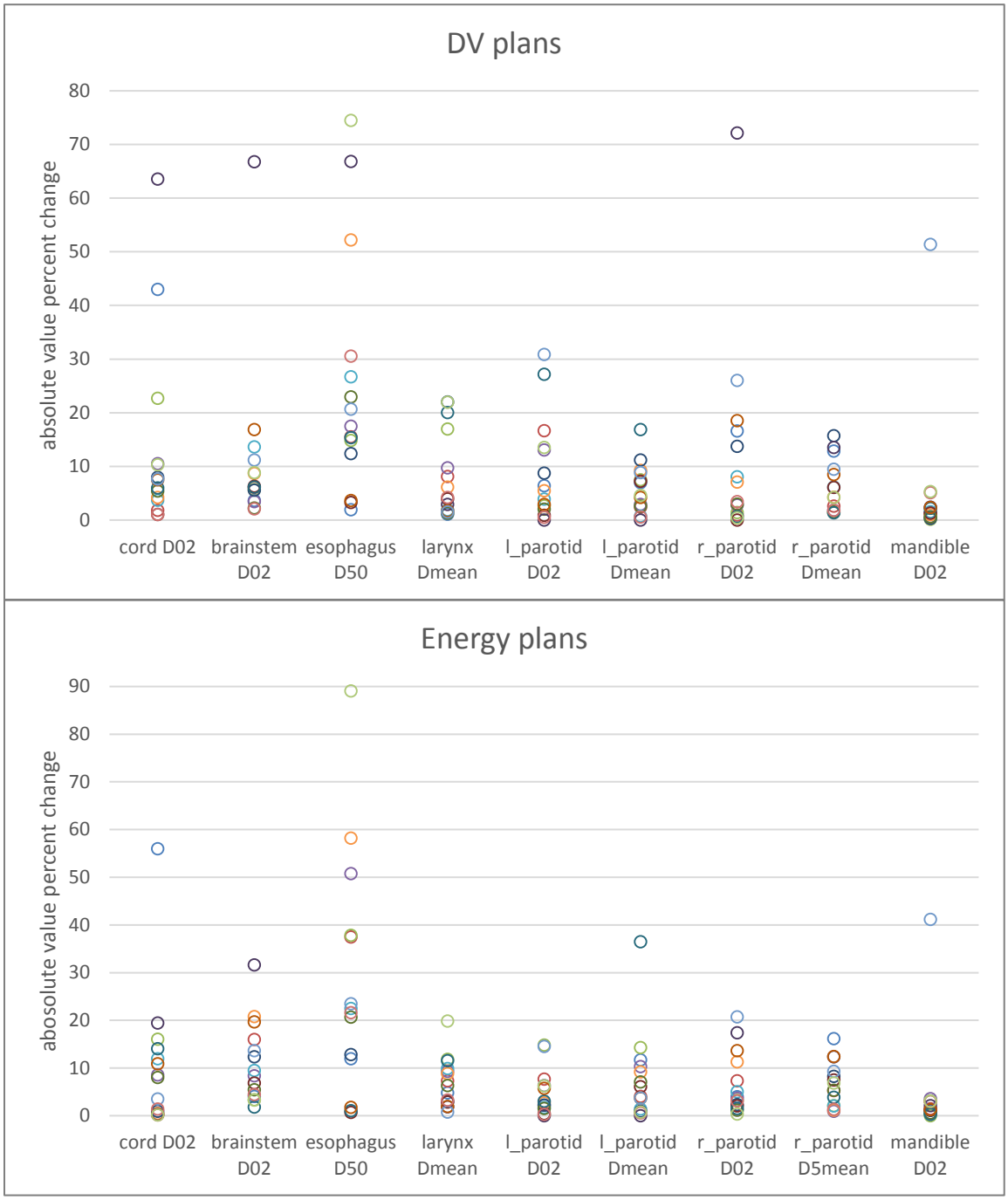

Figure 29. Absolute value percent change of the dose indices (DIs) for each of the 15 patients. The top shows the results for the DV optimized plans and the bottom shows the Energy optimized plans.

4.4 Discussion on Dosimetric Changes due to Changing Anatomy

Three separate studies were performed to determine the sensitivity due to anatomical changes in the course of radiotherapy treatment. The studies focused on looking at mass changes and using density-based inverse optimization compared to that of volume-based inverse optimization for NSCLC and HNSCC. It was hypothesized that density-based inverse optimization plans: DM and Energy would be expected to be more sensitive to changes in anatomy because by going through lower density areas, these might be expected to change the most compared to higher-density (higher-functioning) areas.

The first study demonstrated that mass change of the OARs were not statistically significant. There were large changes in dose to the parotids for some patients as would be expected if there are large changes in anatomy, but the small number of patients in the cohort may not have allowed the establishment of statistically significant findings. The statistically significant lower dose to the PTV mass revealed decreased coverage, which is an undesirable event for radiotherapy effectiveness. Understanding that mass is the product of density and volume, the changes observed in mass are correlated with volume changes. It may have been interesting to look at density changes within the parotids or the tumors during treatment and find how much effect the changes had to DMIs. One study showed that density changes were highly correlated with parotid deformation (Fiorino et al., 2012). The average change in HU was of -7.3 between the last and

the first fraction of treatment. Furthermore, these density changes may be correlated to functional changes as dose to the parotids affect saliva production.

The second study focused on how changes in anatomy affected DM compared to DV inversely optimized plans. In this study it was hypothesized that DM plans would be more sensitive to anatomical changes compared to DVH-base plans. The study was performed by analyzing DIs at the time of planning, mid-treatment, and post-treatment to assess effects during radiotherapy to the target and OARs. Only six patients per anatomical site were analyzed and the results showed a trend of higher sensitivity with DM plans between the planning CT and the post-treatment CT.

Energy-based inverse optimization was also included in this investigation of anatomical changes. The hypothesis was that Energy-based plans would show larger differences than DV plans and even DM plans in this time-trending analysis. Energy-based inverse optimization only uses one objective function per OAR to find a solution to the optimization that depends explicitly on the distribution of density within the volumes. Only the mid-treatment CT was used to analyze the changes in DIs. The changes of the Energy-based plans were not significantly different than DV plans. These suggest that the volume changes correlate to the changes in density within the volume, which has been observed in other studies mentioned previously.

Chapter 5. Mass-weighted Equivalent Uniform Dose

5.1 Generalized Equivalent Uniform Dose (gEUD)

The concept of equivalent uniform dose (EUD) was proposed by Niemierko (1997) and states that "for any dose distribution, the corresponding Equivalent Uniform Dose (EUD) is the dose (in Gy), which, when distributed uniformly across the target volume, causes the survival of the same number of clonogens." This definition was based on the radiobiological concept of surviving fraction at a dose of 2 Gy (SF_2) (Wang et al., 2008). The simplest form of the formula is given in equation 10, where D_{ref} is the reference dose per fraction (2 Gy), D_i is the dose corresponding to a partial volume *i,* and *N* is the number of sub-volumes. Niemierko demonstrated that EUD is linearly related to SF and α/β, and therefore the knowledge of these biological models and parameters are not crucial to estimate EUD, but robust in the underlying definition using them.

$$EUD = D_{ref} \frac{ln[\frac{1}{N}\sum_{i=1}^{N}(SF_2)^{D_i/D_{ref}}]}{ln(SF_2)} \qquad (10)$$

The concept of EUD was expanded by Niemierko (1999) in order to include normal tissues, which came to be defined as the generalized EUD (gEUD) (equation 11). Where v_i is the fraction of the VOI ($v_i = V_i / V_{organ}$) receiving a dose D_i, and *a* is a tissue-specific parameter. This equation is very versatile as can be

used for both tumors and normal tissues. For normal tissues, gEUD represents the amount of uniform dose that will lead to the same probability of injury as a heterogeneous dose distribution. On the other hand, it can represent the amount of uniform dose to a tumor that will lead to the same probability of local control as non-uniform dose (Gay and Niemierko, 2007). The parameter '*a*' defines the model: as its value approaches negative infinity, gEUD approaches the minimum dose. Therefore, negative values are useful for target volumes, since tumor control is dependent on the fraction of the volume receiving the minimum dose, where clonogen survival would be highest. For an *a*-parameter approaching positive infinity, gEUD approaches maximum dose; a larger value is used for serial organs (Allen Li et al., 2012). Serial organs are more affected by maximum doses, as they are perceived as "links in a chain", where if a part of the functional chain is broken, it is responsible for its failure (Gay and Niemierko, 2007). For *a*=1 and *a*=0, gEUD is equivalent to the arithmetic mean dose and geometric mean dose, respectively. Therefore, the *a*-parameter for parallel organs that exhibit large volume effects would be small positive values, **Table 10** summarizes this volume parameter.

$$gEUD = \left(\sum_{i=1}^{N} v_i D_i^a\right)^{1/a} \qquad (6)$$

Table 10. Volume parameter 'a'

Value of a	***gEUD***	***Description***
High (*a* → infinity)	Maximum dose	Serial organs
Low *(a* → - infinity)	Minimum dose	Target
***a* = 1**	Mean dose	Parallel organs

5.2 Mass-Weighted gEUD (mgEUD)

A study (Mavroidis et al., 2006) studied whether DMHs deviated significantly from DVHs regarding lung complications. One of the models used was the Lyman-Kutcher-Burman model, which is a model that correlates normal tissue complication probability to dose. The concept of LKB is further expanded in section 5.3. The parameters used in the model in the mentioned study were from Seppenwoolde et al. (2003) for radiation pneumonitis. Mavroidis et al. found from a theoretical case examined that the tissue response probability using DMHs was lower by 30% compared to DVHs, which is closer to clinically observed response rate.

Having discussed that mass is breathing independent and contributes more information about the irradiated organ, the incorporation of density into the gEUD formulation would provide the equivalent uniform dose to the mass. The mass-weighted gEUD (mgEUD) formulation is shown in equation 12 with mass (m_i). This implementation may lead to a more reliable NTCP value.

$$mgEUD = [\sum_{i=1}^{N} m_i D_i^a]^{1/a} \qquad (7)$$

$$mgEUD = \left[\sum_{i=1}^{N} \left(\frac{\rho_i v_i}{\sum_{k \in V} \rho_k v_k}\right) D_i^a\right]^{1/a} \qquad (8)$$

If the mass term is expanded (equation 13), where ρ_i is the average density in voxel *i* and *k* is just an iterator to sum the whole organ's mass. If the density in

all voxels of the VOI is uniform ($\rho = \rho_i = \rho_k$), equation 12 is simplified to equation 11. Therefore, mgEUD is mathematically more general approach than gEUD, which doesn't take into account density differences. This might be particularly important for lung, where voxels of air exist (low density voxels).

5.2.1 Development of mgEUD Calculation

The calculation of mgEUD was developed by incorporating a calculation plugin (C++ programming language) in a research version of Pinnacle TPS, which is executable from a Pinnacle script. While the plugins are interfaced to the TPS through dynamic link libraries the Pinnacle scripts are special scripting language characteristic to that particular TPS.

Two plugins were developed, one for the calculation of gEUD and one for mgEUD. The following steps were taken for the calculation. First, the density data was obtained from the raw CT data through CT-to-density calibration tables. These tables were obtained from the CT scanner calibration and used to convert CT numbers or Hounsfield units (HU) to electron density. Then to obtain the mass for mgEUD, the corresponding voxel volume was multiplied with the density value characteristic for the voxel. The dose data was obtained from the treatment plan for each voxel. The '*a*' parameter was chosen by the user for the VOI. Finally, the code called for the calculation of the arithmetic equations of gEUD and mgEUD (equation 11 and equation 12).

Pinnacle research version provides a calculated gEUD value, but the underlying calculation method used in the TPS is not transparent; it is unknown how edges of volume contours are defined and how that is accounted for in gEUD calculations. This fact can play a major role in the calculation of gEUD, which is the reason that a script was written for the calculation of gEUD to accurately compare to mgEUD, since they are derived from the same underlying data and the same software. Nonetheless, a check needed to be performed to ensure the reliable values obtained from the computational algorithm. In order to avoid any discrepancy with the volumes, a single CT voxel was contoured as a volume. Three calculations were performed: one gEUD calculation by the TPS, one using the developed software for gEUD, and one using the software for mgEUD. **Table 11** lists the volume, density and results for the two gEUD and mgEUD calculations. As it was expected the gEUD and mgEUD values were equal as the density of the voxel was unity, since as mentioned previously, mgEUD simplifies to gEUD when the density is equal to one. Moreover, the TPS and script gEUD values were equivalent, which validated the calculation software.

Table 11. Values for gEUD and mgEUD script validation

Volume	0.001857 cm^3
Density	1.00 g/cm^3
TPS gEUD	3.0767
Script gEUD	3.0767
Script mgEUD	3.0767

5.3 Normal Tissue Complication Probability Modeling

Before 1991 when the seminal work by Emami et al. (1991) was published including data of partial organ tolerances, physicians relied on experience and intuition to select field and doses for treatment plans. The roots of normal tissue complication probability (NTCP) modeling lie in attempts to quantify dependence of tolerance dose for a certain radiation effect on the size of the treated region (Allen Li et al., 2012). NTCP modeling gained more attention with the development and the widespread application of 3DCRT, which resulted in rather heterogeneous dose distributions in OARs. The complexity of those dose distributions dictated the need to simplify them into a single metric that would correlate to radiation injury risk.

The relationship between the NTCP and dose was first proposed by Lyman (1985) where it was proposed that the relationship is sigmoidal (integrated normal distribution). Equation 14 and equation 15 define Lyman's NTCP, which is essentially an error function of dose and volume. In the equation, parameter TD_{50} is the dose for complication rate of 50% and parameter m is the slope parameter (steepness of the curve increases with decreasing m). The NTCP for partial organ irradiation is based upon clinical estimates of organ tolerance for partial uniform irradiation at different doses and volumes. Following Lyman's publication, Burman et al. (1991) applied the model to clinical tolerance data developed by Emami et al. (1991). This radiobiological model became known as the Lyman-Kutcher-

Burman (LKB) model, which describes complication probabilities using clinical tolerance doses for different irradiated volumes as input data.

The original LKB model applies to treatment plans with uniform partial irradiation, but with multi-field treatment techniques the dose distributions are heterogeneous. Therefore, it was necessary to adapt the Lyman model to a more general form for inhomogeneous dose. One way was using gEUD as it is a dose representative of heterogeneous dose distribution. Equation 16 adapts Lyman's original equation by replacing D with gEUD.

$$\mathrm{NTCP}=\frac{1}{\sqrt{2\pi}}\int_{-\infty}^{t} e^{\frac{-t^2}{2}}\,dt \qquad (9)$$

$$t=\frac{(D-TD_{50})}{m*TD_{50}} \qquad (10)$$

$$t=\frac{(gEUD-TD_{50})}{m*TD_{50}} \qquad (11)$$

A recent study (Semenenko and Li, 2008) used LKB NTCP model with multi-institutional toxicity data for the lung pneumonitis and xerostomia. The results of this study supported the concept of large volume effect for lungs and parotid glands, with estimates of the a-parameter close to unity.

Figure 30 shows the resulting NTCP with respect to mean dose to both lungs. The dashed curve in the graph represents the fit of the LKB model for data including pneumonitis of lower grades, the dash-dot curve is the model for the data

excluding pneumonitis of lower grades, and the solid curve is a fit of the LKB model for the combined dataset. The fitting parameters obtained for the combined dataset were *m*= 0.41 and *TD50*= 29.9 Gy. For xerostomia for the parotid glands, **Figure 31** shows the NTCP LKB model for the obtained datasets. The dashed line is the fit for the parotids as separate organ and the solid curve for the parotids as a single organ. The fitting parameters calculated were m= 0.53 and TD50= 31.4 Gy for the combined organ LKB model.

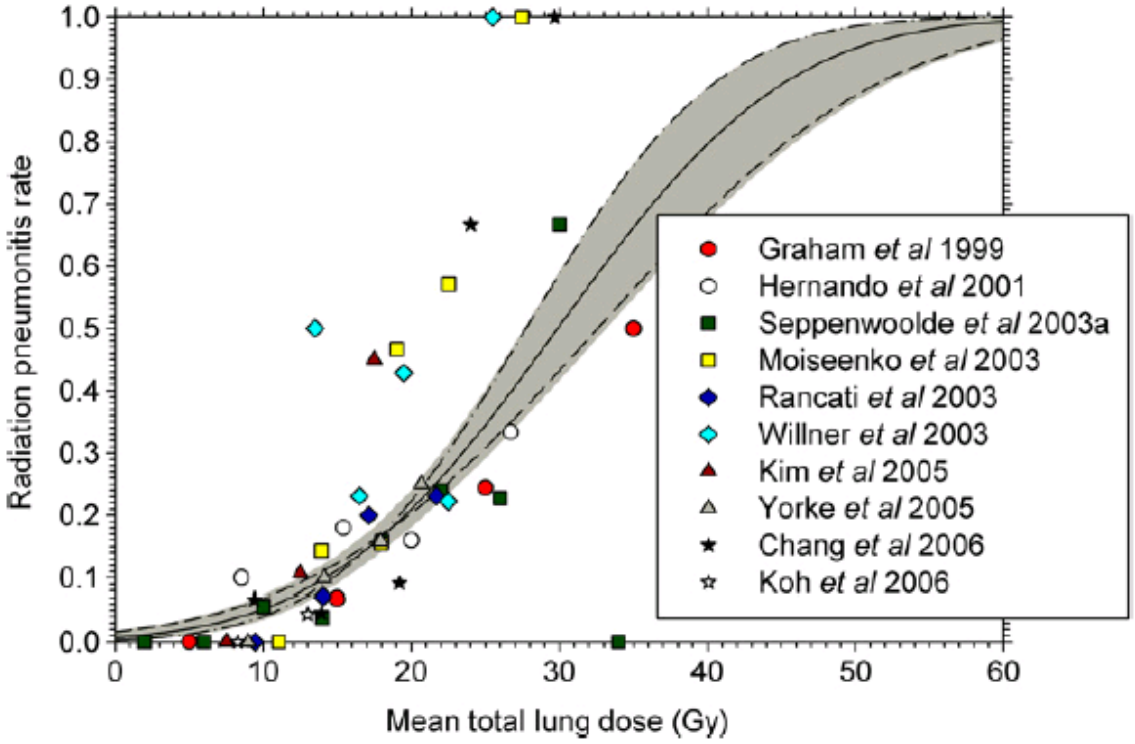

Figure 30.Incidence of radiation pneumonitis as a function of mean dose to the lungs. (Semenenko and Li, 2008)

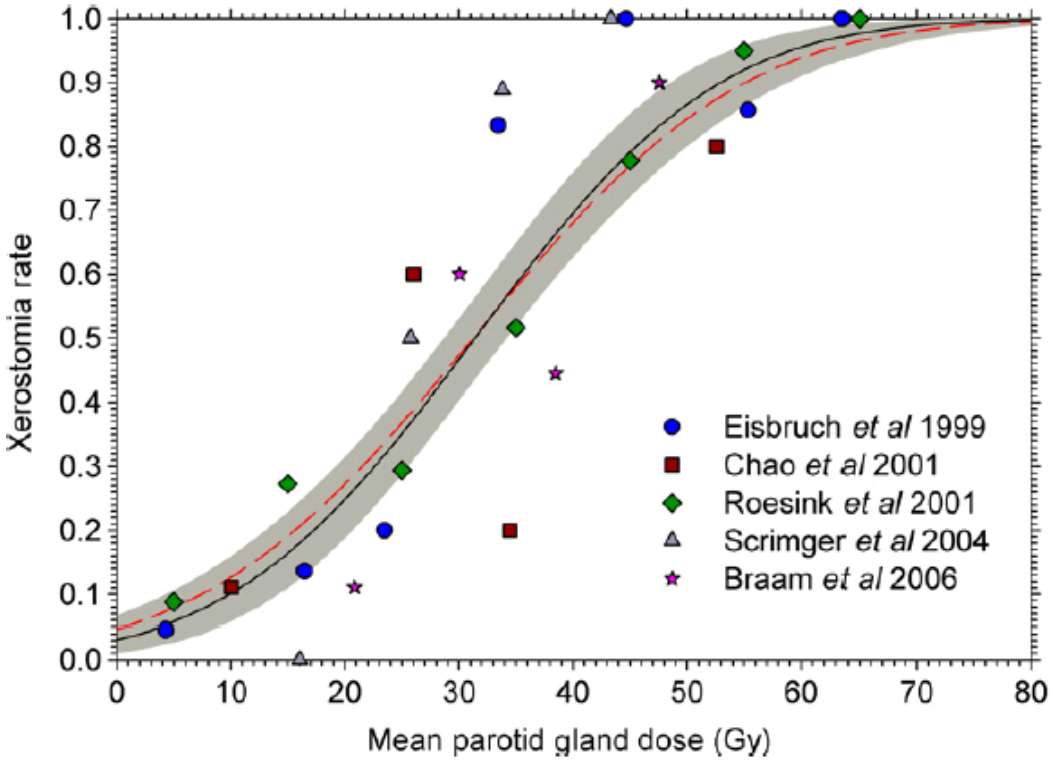

Figure 31. Incidence of xerostomia as a function of mean dose to the parotid gland. (Semenenko and Li, 2008)

The NTCP model has been incorporated into the clinic for evaluation of treatment plans. Although the value is not completely reliable as a standalone value, its use in conjunction with isodose and dose-volume information can help guide decision making in the clinic (Allen Li et al., 2012). **Figure 32** illustrates how from a 3D dose distribution the plan information is reduced to 2D as a DVH and further to a single value such as DI, isovolume, gEUD and subsequently NTCP (Marks et al., 2010).

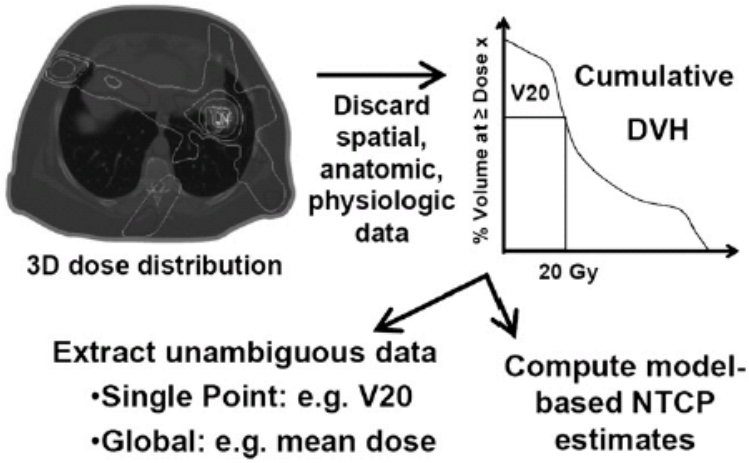

Figure 32. 3D dose distribution is reduced to a 2D DVH, where spatial, anatomic and physiologic data are not carried over. The 2D graph is further reduced to single values of DIs, isovolumes, gEUD and NTCP. (Marks et al., 2010)

Since gEUD can be linked to NTCP, the inclusion of gEUD into a cost function for inverse optimization has been studied. Such studies have shown that gEUD-based inverse optimization reduce the dose to OARs while maintaining adequate target coverage (Wu et al., 2002, Mihailidis et al., 2010, Choi and Deasy, 2002, Mihaylov et al., 2009). Wu et al. (2002) incorporated the gEUD calculation into an objective function for optimization. They compared a prostate case and a head-and-neck case with DVH-based optimization and gEUD-based optimization. The results showed that gEUD-based optimization improved OAR sparing with only a parameter for each OAR as opposed to multiple DV constraints for DVH-based optimization. Mihailidis et al. (2010) applied the same comparison for 10 breast and chest wall IMRT plans and reached the same conclusion.

5.4 HNSCC: NTCP model with gEUD and mgEUD

The purpose of including density and developing mgEUD is to determine if its value correlates better with NTCP compared to gEUD. One of the most observed complications of radiation therapy of HNSCC is xerostomia (dry mouth). Several studies link the mean parotid gland doses to this complication (Chen et al., 2013, Brodin et al., 2018). The purpose of the present study is to determine the difference in mgEUD to gEUD for the parotid glands in patients treated for HNSCC.

5.4.1 Methods and Materials

The treatment plans of fourteen HNSCC patients treated between 2015 and 2017 were transferred from Eclipse TPS (Varian, Palo Alto, CA) to Pinnacle TPS without changes. The target contours were subtracted from the contours of the left and right parotid glands in order to calculate gEUD and mgEUD from the non-target tissue. Using the developed software tools, gEUD and mgEUD were calculated using three values for the volume parameter a= 0.47, 1.0 and 1.1, which were chosen due to differences in published data.

In addition, a correction was made for several treatment plans were not prescribed to 2 Gy per fraction according to equation 17 based on the linear-quadratic cell survival model (Withers et al., 1983). The EUD_x represents the gEUD or mgEUD for the given fractionation x and EUD_{2Gy} is the equivalent gEUD or mgEUD for the fractionation of 2 Gy. The α/β ratio was set to 3 Gy.

$$\mathrm{EUD}_{2\mathrm{Gy}}=\mathrm{EUD}_{\mathrm{x}}\,\frac{\alpha/\beta+\mathrm{x}}{\alpha/\beta+2} \qquad (12)$$

The fourteen patients had toxicity scoring evaluations post radiation therapy. The evaluation included xerostomia grade, which was used to link the gEUD values to complication. The grades were scored according to “Common Terminology Criteria for Adverse Events (CTCAE)” for the adverse event of dry mouth, where grade 0 corresponds to no dry mouth; grade 1 corresponds to symptomatic with slight dryness of mouth; grade 2 corresponds to moderate dryness of mouth and oral intake alterations; grade 3 corresponds to complete dryness of mouth with inability to aliment orally. None of the patients in this study showed xerostomia of grade 3.

5.4.2 Results and Conclusion

The xerostomia grade and the corresponding gEUD and mgUED calculated values are listed in **Table 12**. As can be noted the differences between gEUD and mgEUD for the parotids were very small, regardless of the *a*-parameter used. Some mgEUD values were smaller than gEUD, while others were larger.

Ultimately, for illustration purposes, a plot for each of the three *a*-parameters for gEUD and mgEUD with respect to xerostomia grade are shown in **Figure 33**. In addition, the mean and standard deviation for both EUD values are listed on **Table 13**, where the highest variability of values tends to be in grade 1.

Furthermore, there was a trend of slightly smaller standard deviation for mgEUD for grades 1 and 2, but the trend was reversed for grade 0 for all the a-parameters.

The results of this study show that the inclusion of density for gEUD calculation (mgEUD) is not indicative of a significant change in the value. Most organs tend to have very small differences in density within, making the average density unity. Larger differences are expected from more heterogeneous volumes, such as lungs.

Table 12. Values for gEUD and mgEUD and the percent difference between the two values for each a-parameter used (0.47, 1.0, and 1.1)

		***a*=0.47**			***a*=1.0**			***a*=1.1**		
Pt #	**Xerostomia Grade**	**gEUD**	**mgEUD**	**percent difference**	**gEUD**	**mgEUD**	**percent diff**	**gEUD**	**mgEUD**	**percent difference**
1	**0**	2.48	2.51	1.22	3.46	3.51	1.21	3.67	3.72	1.19
2	**0**	2.18	2.16	-0.83	4.17	4.13	-0.90	4.57	4.53	-0.89
3	**0**	4.26	4.28	0.43	6.14	6.17	0.36	6.54	6.56	0.35
4	**1**	9.26	9.29	0.40	9.35	9.39	0.40	9.37	9.41	0.40
5	**1**	14.95	14.94	-0.07	16.22	16.21	-0.07	16.49	16.47	-0.07
6	**1**	9.68	9.73	0.53	11.98	12.05	0.53	12.42	12.49	0.53
7	**1**	18.77	18.76	-0.08	20.64	20.62	-0.08	21.00	20.99	-0.09
8	**1**	9.89	9.85	-0.34	11.31	11.27	-0.37	11.63	11.58	-0.38
9	**1**	5.76	5.79	0.51	7.95	7.98	0.43	8.34	8.38	0.42
10	**2**	15.89	15.79	-0.65	18.73	18.63	-0.54	19.23	19.13	-0.52
11	**2**	15.15	15.06	-0.60	17.15	17.04	-0.62	17.56	17.46	-0.62
12	**2**	11.08	11.08	-0.04	12.14	12.14	-0.03	12.35	12.34	-0.03
13	**2**	16.96	16.89	-0.40	18.59	18.51	-0.40	18.91	18.83	-0.39
14	**2**	16.14	16.20	0.36	18.27	18.33	0.33	18.67	18.73	0.31

Table 13. Mean and standard deviation of the gEUD and mgEUD values divided into xerostomia grade outcomes.

	gEUD (a=0.47)		***mgEUD (a=0.47)***		***gEUD (a=1.0)***		***mgEUD (a=1.0)***		***gEUD (a=1.1)***		***mgEUD (a=1.1)***	
Grade	**mean**	**SD**	**mean**	**SD**	**mean**	**SD**	**mean**	**SD**	**mean**	**SD**	**mean**	**SD**
0	2.97	1.12	2.98	1.13	4.59	1.39	4.60	1.39	4.93	1.47	4.94	1.46
1	11.38	4.66	11.39	4.64	12.91	4.72	12.92	4.70	13.21	4.76	13.22	4.74
2	15.04	2.31	15.00	2.29	16.98	2.77	16.93	2.75	17.34	2.86	17.30	2.84

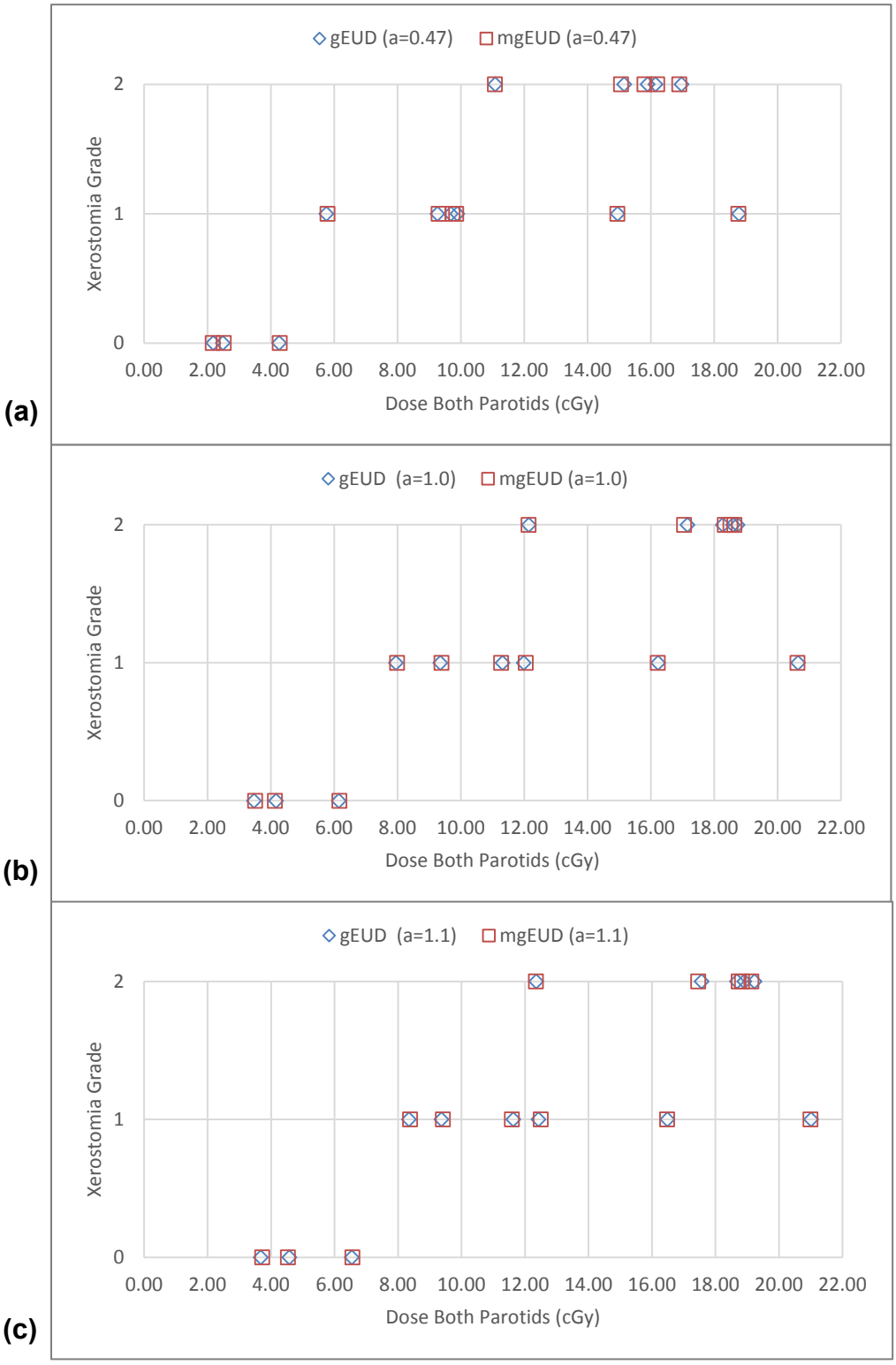

Figure 33. Values of gEUD and mgEUD with respect to xerostomia grade for (a) a= 0.47, (b) a= 1.0, and (c) a= 1.1.

5.5 NSCLC: NTCP model with gEUD and mgEUD

The probability of developing radiation pneumonitis after treatment with high-dose radiotherapy is important for patients with NSCLC. Severe radiation pneumonitis in the first six months after radiation therapy may be life threatening. Patients who survive the pneumonitis phase may translate on to the type and severity of subsequent late response (Seppenwoolde et al., 2003). It is therefore essential to understand the doses that aggravate this complication. Several studies have investigated the correlation of gEUD and incidence of pneumonitis, with LKB model being the best fitting NTCP model (Ioannis et al., 2007).

5.5.1 Methods and Materials

Treatment plans of twenty-one patients who were treated for NSCLC between early 2014 and late 2016 were gathered and transferred from Eclipse TPS to Pinnacle TPS. As in section 5.4.1, the treatment plans were transferred without changes to contours or doses. The target contours were subtracted from both lungs and both EUD values were calculated. The calculation of these values was performed with the developed software, the a-parameters used were 1.0, 1.1 and 1.2, as previously published data has used different values. The best fitting a-parameter was determined for this data. A paired two-tailed t-test was performed to determine if differences between mgEUD and gEUD values were statistical significance ($p \leq 0.05$).

Pneumonitis grading was based on CTCAE with grade 0 meaning no symptoms nor clinical observation. Grade 1 corresponded to patients without symptoms with diagnostic observation. Grade 2 was for symptomatic patients with necessary medical intervention with prescribed steroids. Finally, grade 3 was associated with severe symptoms, steroids prescribed and oxygen indicated. Grades 4 corresponded to life-threatening symptoms and ventilation support and grade 5 to death, respectively. None of the patients in the patient cohort exhibited pneumonitis grades 4 or 5.

In the same way as for the previous study for the parotid glands (section 5.4.1), gEUD and mgEUD were corrected for fractionation schedule (c.f. *equation 14*). Subsequently, the values were divided into subgroups of 2 Gy bins. The corresponding probability of developing pneumonitis Grade ≥ 2 was calculated for the patient cohort. To perform the curve fitting according to LKB (equation 14) and determine the best fitting parameters MATLAB R2017a Curve Fitting Toolbox (The MathWorks, Natick, MA) was used.

5.5.2 Results and Conclusion

The calculated values for gEUD and mgEUD with the corresponding percent differences are listed in **Table 14**. The values increased with increasing a-parameter, as is expected due to the definition. The mgEUD value was always higher for pneumonitis grade 0, but this trend was not observed for the higher pneumonitis grades. Half of the patients with grade 1 pneumonitis had higher

mgEUD values compared to gEUD. Six out of nine patients with outcomes of grade 2 showed a lower mgEUD value than gEUD. No statistical significant differences were found between gEUD and mgEUD.

The results are presented in **Figure 34**, were the ordinate is the pneumonitis grade level and the abscissa the dose to both lungs minus the planning target volume. From the figure it can be observed the mgEUD values are clustered closer for each pneumonitis grade compared to gEUD values. In order to quantify this variability of the gEUDs and the mgEUDs, the mean and standard deviation of the sample cohort were calculated for each grade (c.f. **Table 15**) and each tallied quantity. Even though the values of gEUD and mgEUD were close, the standard deviation for mgEUD for grades ≥ 1 were consistently smaller.

Table 14. Values for gEUD and mgEUD and the percent difference between the two values for each a-parameter used (1.0, 1.1, and 1.2)

	a=1.0			***a=1.1***			***a=1.2***		
Pneumonitis Grade	**gEUD**	**mgEUD**	**% diff**	**gEUD**	**mgEUD**	**% diff**	**gEUD**	**mgEUD**	**% diff**
0	11.64	11.86	1.96	12.06	12.30	1.95	12.48	12.72	1.92
0	12.64	12.82	1.40	13.36	13.56	1.50	14.06	14.28	1.59
0	15.27	16.27	6.54	15.87	16.90	6.44	16.47	17.51	6.34
0	5.22	5.84	11.92	6.01	6.74	12.01	6.85	7.68	12.02
1	7.53	8.37	11.13	7.92	8.79	11.03	8.32	9.23	10.88
1	8.62	8.45	-1.94	9.26	9.11	-1.65	9.91	9.78	-1.39
1	9.99	10.29	2.99	10.78	11.10	2.98	11.54	11.88	2.95
1	10.46	10.41	-0.53	11.09	11.06	-0.29	11.73	11.72	-0.09
2	15.30	12.52	-18.15	16.01	13.30	-16.92	16.70	14.06	-15.78
2	12.23	11.64	-4.76	12.86	12.26	-4.66	13.48	12.87	-4.54
2	13.59	12.87	-5.25	14.23	13.52	-4.99	14.87	14.17	-4.74
2	11.13	12.08	8.57	11.94	12.99	8.79	12.77	13.91	8.93
2	14.83	14.92	0.66	15.71	15.87	0.97	16.60	16.80	1.22
2	17.05	15.66	-8.11	17.70	16.34	-7.69	18.35	17.42	-5.08
2	8.29	9.00	8.53	8.99	9.78	8.83	9.69	10.57	9.05
2	9.18	8.49	-7.54	9.78	9.11	-6.88	10.38	9.73	-6.29
2	13.59	13.38	-1.54	14.09	13.89	-1.41	14.57	14.38	-1.30
3	18.04	18.35	1.70	18.87	19.20	1.74	19.69	20.04	1.77
3	16.44	14.66	-10.83	17.06	15.34	-10.08	17.66	16.00	-9.40
3	7.99	8.15	1.97	8.56	8.71	1.77	9.12	9.26	1.60
3	8.95	9.45	5.59	9.89	10.43	5.46	10.84	11.41	5.30

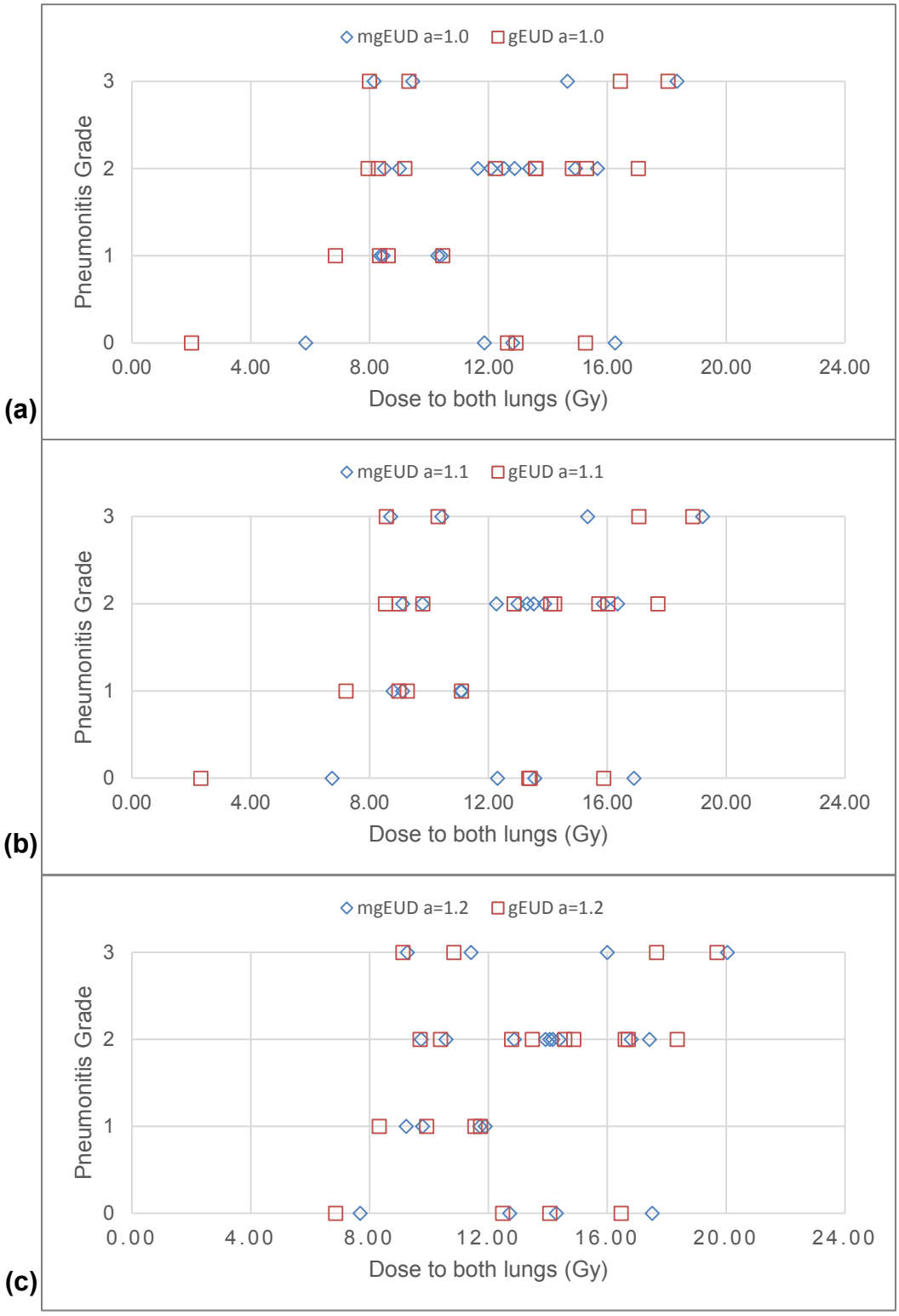

Figure 34. Results for gEUD and mgEUD with respect to pneumonitis grade outcome for three a-parameter values: (a) 1=1.0, (b) a=1.1, and (c) a= 1.2.

Table 15. Mean and standard deviation of the gEUD and mgEUD values divided into pneumonitis grade outcomes.

Pneumonitis Grade		a= 1.0		a= 1.1		a= 1.2	
		gEUD	mgEUD	gEUD	mgEUD	gEUD	mgEUD
Grade 0	**mean**	11.19	11.70	11.83	12.37	12.46	13.05
	SD	4.26	4.34	4.19	4.23	4.08	4.10
Grade 1	**mean**	9.15	9.38	9.76	10.01	10.38	10.65
	SD	1.33	1.12	1.47	1.24	1.59	1.35
Grade 2	**mean**	12.80	12.29	13.48	13.01	14.16	13.77
	SD	2.88	2.39	2.89	2.41	2.90	2.51
Grade 3	**mean**	12.85	12.65	13.60	13.42	14.33	14.18
	SD	5.12	4.73	5.13	4.77	5.14	4.81

After performing the curve fitting program using LKB NTCP model (c.f. equation 13 and equation 15) the best fitting a-parameter was 1.2 for both gEUD and mgEUD. **Table 16** lists the fitting parameters obtained and the corresponding coefficient of determination (R^2). This statistical value is the proportion of the variance in the dependent variable that is predictable from the independent variable. An R^2 with a value of 0 means that the dependent variable cannot be predicted from the independent variable and a value of 1 means that the dependent variable can be predicted without error from the independent variable. Therefore, the closer the R^2 value is to one, the better the fit. The curve fit is shown in **Figure 35**, where both gEUD and mgEUD are plotted with respect to NTCP (pneumonitis Grade ≥ 2) for the three a-parameters. It is also evident from the curve and the corresponding probabilities that the parameter a=1.2 resulted in the closest fit. Moreover, the plot illustrates that the curves for a-values 1.1 and 1.2

were very close, but the obtained probabilities were more closely represented with a-parameter of 1.2. It can also be noted that for mgEUD curves with a=1.1 and a=1.2 the curves started diverging after about 8 Gy. The differences between gEUD and mgEUD for a= 1.2 curves was in the range of 2-3% beyond about 10 Gy. In addition, mgEUD a= 1.0 curve differs from the rest and this is due to one patient plan who had a dose to both lungs of 16.27 Gy with Grade 0 pneumonitis and the only data point for the dose bin, which explains the reason for a worse R^2 value of the curve fit.

Table 16. Results of the best fitting parameters TD50 and m for gEUD and mgEUD with three a-parameters. Coefficient of determination (R^2) for the three a-parameter values for both gEUD and mgEUD.

	gEUD			**mgEUD**		
	TD50	***m***	***R^2***	***TD50***	***m***	***R^2***
***a* = 1.0**	9.01	0.6486	0.7473	10.70	0.8661	0.2058
***a* = 1.1**	10.61	0.4753	0.6636	10.71	0.4814	0.6731
***a* = 1.2**	10.56	0.4724	0.8736	10.37	0.4633	0.8563

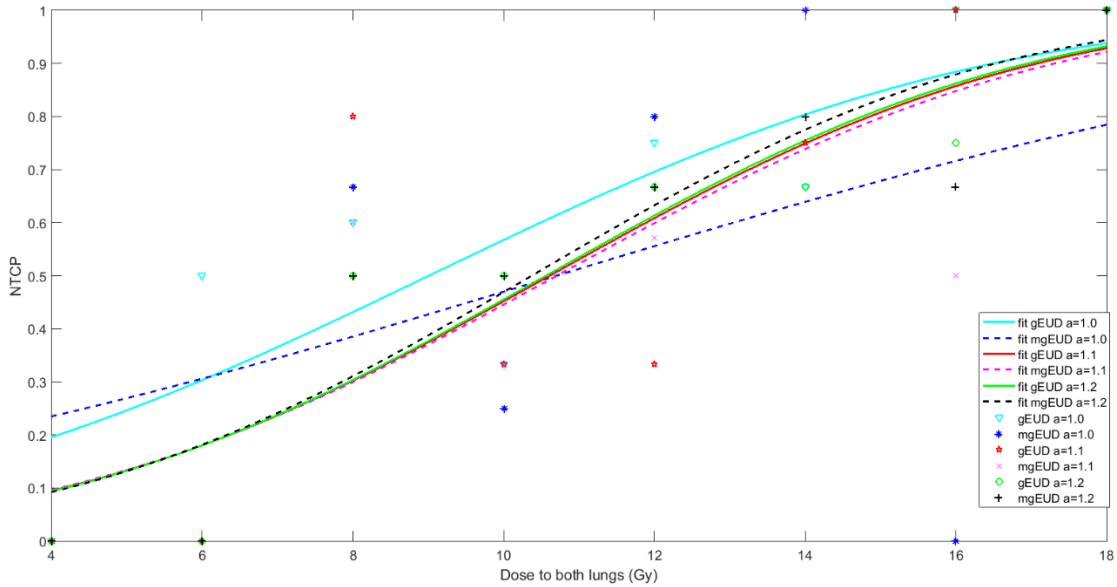

Figure 35. Curve fitting according to probability of developing pneumonitis with Grade 2 or higher with respect to gEUD and mgEUD with three a-parameters.

5.6 Discussion on mgEUD and NTCP

The inclusion of density in the mgEUD formulation (equation 10) represents a more general mathematical form of gEUD (equation 9). After developing software and implementing it as a plugin to calculate mgEUD and gEUD, the next step was to link the value to NTCP in order to find the validity of the new equation. This was done by using treatment plans from previously treated patients with HNSCC and NSCLC. Two studied dose limiting organs that commonly exhibit complications are parotid glands and lungs for HNSCC and NSCLC, respectively.

First the parotid xerostomia outcome data was evaluated. The values for mgEUD compared to gEUD were very similar. There were only 14 patient cases with documented complications, which might have been insufficient for establishing statistical significance. Nonetheless, since there was no trend observed, it can be concluded that mgEUD formulation does not contribute further information than gEUD formulation for the parotid glands.

Lungs are more heterogeneous than the parotids and it was hypothesized that the effect might be larger. The differences between gEUD and mgEUD were larger, but without statistical significance. At pneumonitis grade ≥ 2, the mgEUD values had smaller standard deviation. Smaller variations of mgEUDs suggested that mgEUD concept could yield a better predictive model for the observed toxicity. There were two approaches to present the data; the first was plotting the values of gEUD and mgEUD for each patient according to the pneumonitis grade outcome. This is where the tendency for mgEUD values to be clustered closer is observed (Figure 37).The second was using the probability that a patient in the cohort would develop pneumonitis grade ≥ 2, with which the LKB model was based on. For a small patient cohort the first presentation of the data seems more representative of the differences between gEUD and mgEUD. Comparing the data obtained in this study as with previously published data, illustrated in Figure 32, it is evident that a lot of the data is clustered in the lower dose end (≤ 20 Gy). Furthermore, the a-parameter that resulted in the best curve fit for both gEUD and mgEUD was 1.2. The limitation of this study was the small number of patients. A larger patient cohort

would possibly yield a better representation of the probability and may in turn show more robust differences between gEUD and mgEUD for the lungs.

Chapter 6. Summary

This dissertation involved exploring the effects of including density in the inverse optimization cost function when changing IMRT delivery parameters and when patient anatomy changes during radiotherapy. The two anatomical sites for which the studies were conducted were HNSCC and NSCLC. Including density information in the cost function gives the optimizer the mass information of the volumes rather than just the volume information. Two types of density-based optimization which are called DM and Energy were investigated.

The effect of changing IMRT segment delivery parameters of number of allowed segments per beam and minimum segment area was studied for both DM and Energy inverse optimization modalities. In order to better determine the effect of the parameter changes, twelve HNSCC and twelve NSCLC patient plans were used to retrospectively develop eight plans per patient, four plans per parameter combination (number of segments per beam and segment area). For each combination, three optimization approaches were used: DV, DM, and Energy. All plans were optimized using the same approach, which involved setting the nine equidistant beams around the target to deliver the prescription dose. Then, iteratively, dose to the surrounding OARs was reduced until the same standard deviation of the dose across the target was met. All plans were normalized such that the targets received the prescribed doses. The results showed that Energy plans were significantly more sensitive to changing delivery parameters compared to DM plans and DV plans.

Moreover, for changing anatomy with the progression of radiotherapy, the first study looking at the changes in OAR DMIs did not show significant differences between CTs (mid-treatment and post-treatment) compared to the planning CT. There were statistically significant changes to PTV coverage, which would need to be addressed to meet the dose prescription. The subsequent two studies determined that sensitivity of DM and Energy optimizations compared to the sensitivity of DV for the changing anatomy was not statistically significantly different. For DM plans some tendency was observed as the changes for some DIs were larger, but no definitive conclusion could be reached. An important factor that steered some of the results was the positioning of the patient for the subsequent CTs; it was observed that in one case that a small tilt of the head position resulted in a dose increase to almost 300% to 50% of the esophagus. In conclusion, it was shown that DM and Energy plans have comparable sensitivity to DV plans with changing patient anatomy.

Finally, the effect of density inclusion in the calculation of NTCP was investigated. A plugin in Pinnacle TPS was developed and tested in order to calculate gEUD and mgEUD. The gEUDs and the mgEUDs were used in a widely employed LKB model for normal tissue toxicity evaluation. The software was used to evaluate gEUD and mgEUD for two OARs: parotid glands and lungs. Fourteen patients with xerostomia grade outcome were used to calculate the two values for both parotids in conjunction. The differences between gEUD and mgEUD were very small and it was concluded that the addition of the density term did not affect

the gEUD formalism for the parotids. The lung gEUD and mgEUD values displayed larger differences, but were not statistically significant. The standard deviation of the mgEUD doses for pneumonitis grades 1, 2 and 3 were smaller than for gEUD, which may become more significant with a larger patient cohort. The best fitting a-parameter was found to be 1.2. Since the differences EUD values were not statistically significant, the fitting was not either but did show some differences.

Looking forward, the addition of more patients to the NSCLC patient cohort for mgEUD analysis may be of interest. The largest drawback of the work presented herein is that only 21 patient plans were used. Therefore, in order to achieve more robust modelling, more patients need to be included. Upon demonstration of mgEUD and its difference with gEUD, it may be valuable to include mgEUD into the inverse optimization cost function.

References

Aaltonen, P., Brahme, A., Lax, I., Levernes, S., Näslund, I., Reitan, J. B. & Turesson, I. 1997. Specification of Dose Delivery in Radiation Therapy. Recommendations by the Nordic Association of Clinical Physics (NACP). *Acta Oncologica,* 36**,** 1-32.

Abdulla, S. 2018. *Ct Equipment* [Online]. Available: https://www.radiologycafe.com/radiology-trainees/frcr-physics-notes/ct-equipment [Accessed March 16, 2018].

Ahnesjö, A., Hårdemark, B., Isacsson, U. & Montelius, A. 2006. The IMRT information process—mastering the degrees of freedom in external beam therapy. *Physics in Medicine and Biology,* 51**,** R381.

Alberg, A. J., Brock, M. V., Ford, J. G., Samet, J. M. & Spivack, S. D. 2013. Epidemiology of Lung Cancer: Diagnosis and Management of Lung Cancer, 3rd ed: American College of Chest Physicians Evidence-Based Clinical Practice Guidelines. *Chest,* 143**,** e1S-e29S.

Allen Li, X., Alber, M., Deasy, J. O., Jackson, A., Ken Jee, K.-W., Marks, L. B., Martel, M. K., Mayo, C., Moiseenko, V., Nahum, A. E., Niemierko, A., Semenenko, V. A. & Yorke, E. D. 2012. The use and QA of biologically related models for treatment planning: Short report of the TG-166 of the therapy physics committee of the AAPM a). *Medical Physics,* 39**,** 1386-1409.

American Cancer Society. 2016. *What Is Non-Small Cell Lung Cancer?* [Online]. American Cancer Society. Available: https://www.cancer.org/cancer/non-small-cell-lung-cancer/about/what-is-non-small-cell-lung-cancer.html [Accessed 9 March 2018 2018].

Arthur Boyer, P. B., James Galvin, Eric Klein, Thomas LoSasso, Daniel Low, Katherine Mah, Cedric Yu 2001. AAPM TG 72: Basic applications of multileaf collimators. *Medical Physics*.

Ballivy, O., Parker, W., Vuong, T., Shenouda, G. & Patrocinio, H. 2006. Impact of geometric uncertainties on dose distribution during intensity modulated radiotherapy of head-and-neck cancer: the need for a planning target volume and a planning organ-at-risk volume. *Current Oncology,* 13**,** 108-115.

Barker Jr, J. L., Garden, A. S., Ang, K. K., O'Daniel, J. C., Wang, H., Court, L. E., Morrison, W. H., Rosenthal, D. I., Chao, K. S. C., Tucker, S. L., Mohan, R. & Dong, L. 2004. Quantification of volumetric and geometric changes occurring during fractionated radiotherapy for head-and-neck cancer using an integrated CT/linear accelerator system. *International Journal of Radiation Oncology*Biology*Physics,* 59**,** 960-970.

Barkley Jr, H. T. & Fletcher, G. H. 1977. The significance of residual disease after external irradiation of squamous cell carcinoma of the oropharynx. *Radiology,* 124**,** 493-495.

Barnett, G. C., West, C. M. L., Dunning, A. M., Elliott, R. M., Coles, C. E., Pharoah, P. D. P. & Burnet, N. G. 2009. Normal tissue reactions to radiotherapy: towards tailoring treatment dose by genotype. *Nature reviews. Cancer,* 9**,** 134-142.

Bates, E. L., Bragg, C. M., Wild, J. M., Hatton, M. Q. F. & Ireland, R. H. 2009. Functional image-based radiotherapy planning for non-small cell lung cancer: A simulation study. *Radiotherapy and Oncology,* 93**,** 32-36.

Bernier, J. 2009. Current state-of-the-art for concurrent chemoradiation. *Seminars in Radiation Oncology,* 19**,** 3-10.

Bernier, J. & Bentzen, S. M. 2003. Altered fractionation and combined radio-chemotherapy approaches: Pioneering new opportunities in head and neck oncology. *European Journal of Cancer,* 39**,** 560-571.

Bortfeld, T. 2006. IMRT: a review and preview. *Physics in Medicine and Biology,* 51**,** R363.

Bortfeld, T. R., Kahler, D. L., Waldron, T. J. & Boyer, A. L. 1994. X-ray field compensation with multileaf collimators. *International Journal of Radiation Oncology*Biology*Physics,* 28**,** 723-730.

Bosmans, G., van Baardwijk, A., Dekker, A., Öllers, M., Boersma, L., Minken, A., Lambin, P. & De Ruysscher, D. 2006. Intra-patient variability of tumor volume and tumor motion during conventionally fractionated radiotherapy for locally advanced non-small-cell lung cancer: A prospective clinical study. *International Journal of Radiation Oncology*Biology*Physics,* 66**,** 748-753.

Bradley, J. D., Moughan, J., Graham, M. V., Byhardt, R., Govindan, R., Fowler, J., Purdy, J. A., Michalski, J. M., Gore, E. & Choy, H. 2010. A phase I/II radiation dose escalation study with concurrent chemotherapy for patients with inoperable stages I to III non-small-cell lung cancer: phase I results of RTOG 0117. *International Journal of Radiation Oncology*Biology*Physics,* 77**,** 367-72.

Brahme, A., Roos, J. E. & Lax, I. 1982. Solution of an integral equation encountered in rotation therapy. *Physics in Medicine and Biology,* 27**,** 1221-9.

Britton, K. R., Starkschall, G., Liu, H., Chang, J. Y., Bilton, S., Ezhil, M., John-Baptiste, S., Kantor, M., Cox, J. D., Komaki, R. & Mohan, R. 2009. Consequences of anatomic changes and respiratory motion on radiation dose distributions in conformal radiotherapy for locally advanced non–small-cell lung cancer. *International Journal of Radiation Oncology*Biology*Physics,* 73**,** 94-102.

Britton, K. R., Starkschall, G., Tucker, S. L., Pan, T., Nelson, C., Chang, J. Y., Cox, J. D., Mohan, R. & Komaki, R. 2007. Assessment of gross tumor volume regression and motion changes during radiotherapy for non-small-cell lung cancer as measured by four-dimensional computed tomography. *International Journal of Radiation Oncology*Biology*Physics,* 68**,** 1036-1046.

Brodin, N. P., Kabarriti, R., Garg, M. K., Guha, C. & Tome, W. A. 2018. Systematic review of normal tissue complication models relevant to standard fractionation radiation therapy of the head and neck region published after the quantec reports. *International Journal of Radiation Oncology*Biology*Physics,* 100**,** 391-407.

Brown, J. M. & Adler, J. R., Jr. 2015. Is equipment development stifling innovation in radiation oncology? *International Journal of Radiation Oncology*Biology*Physics,* 92**,** 713-714.

Burman, C., Kutcher, G. J., Emami, B. & Goitein, M. 1991. Fitting of normal tissue tolerance data to an analytic function. *International Journal of Radiation Oncology*Biology*Physics,* 21**,** 123-135.

Castadot, P., Lee, J. A., Geets, X. & Grégoire, V. 2010. Adaptive radiotherapy of head and neck cancer. *Seminars in Radiation Oncology,* 20**,** 84-93.

Chen, W.-C., Lai, C.-H., Lee, T.-F., Hung, C.-H., Liu, K.-C., Tsai, M.-F., Wang, W.-H., Chen, H., Fang, F.-M. & Chen, M.-F. 2013. Scintigraphic assessment of salivary function after intensity-modulated radiotherapy for head and neck cancer: Correlations with parotid dose and quality of life. *Oral Oncology,* 49**,** 42-48.

Cheong, K.-H., Kang, S.-K., Lee, M., Kim, H., Bae, H., Park, S., Hwang, T., Kim, K. & Han, T. 2013. Analytic study on the effects of the number of MLC segments and the least segment area on step-and-shoot head-and-neck IMRT planning using direct machine parameter optimization. *Journal of the Korean Physical Society,* 62**,** 1330-1339.

Choi, B. & Deasy, J. O. 2002. The generalized equivalent uniform dose function as a basis for intensity-modulated treatment planning. *Physics in Medicine and Biology,* 47**,** 3579.

De Jaeger, K., Seppenwoolde, Y., Boersma, L. J., Muller, S. H., Baas, P., Belderbos, J. S. & Lebesque, J. V. 2003. Pulmonary function following high-dose radiotherapy of non-small-cell lung cancer. *International Journal of Radiation Oncology*Biology*Physics,* 55**,** 1331-40.

Derbyshire, S. J., Morgan, A. M., Thompson, R. C. A., Henry, A. M. & Thwaites, D. I. 2009. Optimal planning parameters for simultaneous boost IMRT treatment of prostate cancer using a Beam Modulator™. *Reports of Practical Oncology and Radiotherapy,* 14**,** 205-213.

Dobler, B., Koelbl, O., Bogner, L. & Pohl, F. 2009. Direct machine parameter optimization for intensity modulated radiation therapy (IMRT) of oropharyngeal cancer – a planning study. *Journal of Applied Clinical Medical Physics,* 10**,** 4-15.

Drzymala, R. E., Mohan, R., Brewster, L., Chu, J., Goitein, M., Harms, W. & Urie, M. 1991. Dose-volume histograms. *International Journal of Radiation Oncology*Biology*Physics,* 21**,** 71-78.

Emami, B., Lyman, J., Brown, A., Cola, L., Goitein, M., Munzenrider, J. E., Shank, B., Solin, L. J. & Wesson, M. 1991. Tolerance of normal tissue to therapeutic irradiation. *International Journal of Radiation Oncology*Biology*Physics,* 21**,** 109-122.

Erridge, S. C., Seppenwoolde, Y., Muller, S. H., Van Herk, M., De Jaeger, K., Belderbos, J. S. A., Boersma, L. J. & Lebesque, J. V. 2003. Portal imaging to assess set-up errors, tumor motion and tumor shrinkage during conformal radiotherapy of non-small cell lung cancer. *Radiotherapy and Oncology,* 66**,** 75-85.

Ettinger, D. S., Wood, D. E., Akerley, W., Bazhenova, L. A., Borghaei, H., Camidge, D. R., Cheney, R. T., Chirieac, L. R., D'Amico, T. A., Demmy, T. L., Dilling, T. J., Govindan, R., Grannis, F. W., Jr., Horn, L., Jahan, T. M., Komaki, R., Kris, M. G., Krug, L. M., Lackner, R. P., Lanuti, M., Lilenbaum, R., Lin, J., Loo, B. W., Jr., Martins, R., Otterson, G. A., Patel, J. D., Pisters, K. M., Reckamp, K., Riely, G. J., Rohren, E., Schild, S., Shapiro, T. A., Swanson, S. J., Tauer, K., Yang, S. C., Gregory, K. & Hughes, M. 2014. Non-small cell lung cancer, version 1.2015. *Journal of the National Comprehensive Cancer Network,* 12**,** 1738-61.

Evans, E. S., Hahn, C. A., Kocak, Z., Zhou, S.-M. & Marks, L. B. 2007. The role of functional imaging in the diagnosis and management of late normal tissue injury. *Seminars in Radiation Oncology,* 17**,** 72-80.

Ezzell, G. A., Galvin, J. M., Low, D., Palta, J. R., Rosen, I., Sharpe, M. B., Xia, P., Xiao, Y., Xing, L. & Yu, C. X. 2003. Guidance document on delivery, treatment planning, and clinical implementation of IMRT: Report of the IMRT subcommittee of the AAPM radiation therapy committee. *Medical Physics,* 30**,** 2089-2115.

Fiorino, C., Rizzo, G., Scalco, E., Broggi, S., Belli, M. L., Dell'Oca, I., Dinapoli, N., Ricchetti, F., Rodriguez, A. M., Di Muzio, N., Calandrino, R., Sanguineti, G., Valentini, V. & Cattaneo, G. M. 2012. Density variation of parotid glands during IMRT for head-and-neck cancer: Correlation with treatment and anatomical parameters. *Radiotherapy and Oncology,* 104**,** 224-229.

Fox, J., Ford, E., Redmond, K., Zhou, J., Wong, J. & Song, D. Y. 2009. Quantification of tumor volume changes during radiotherapy for non-small-cell lung cancer. *International Journal of Radiation Oncology*Biology*Physics,* 74**,** 341-348.

Gay, H. A. & Niemierko, A. 2007. A free program for calculating EUD-based NTCP and TCP in external beam radiotherapy. *Physica Medica,* 23**,** 115-125.

Graham, M. V., Purdy, J. A., Emami, B., Harms, W., Bosch, W., Lockett, M. A. & Perez, C. A. 1999. Clinical dose–volume histogram analysis for pneumonitis after 3D treatment for non-small cell lung cancer (NSCLC). *International Journal of Radiation Oncology*Biology*Physics,* 45**,** 323-329.

Hårdemark, B. L., Anders; Rehbinder,Henrik ; Löf, Johan 2003. P3IMRT. Direct machine parameter optimization. *White Paper.* Phillips Medical Systems.

Howlader, N., Noone, A., Krapcho, M., Miller, D., Bishop, K., Kosary, C., Yu, M., Ruhl, J., Tatalovich, Z., Mariotto, A., Lewis, D., Chen, H., Feuer, E. & Cronin, K. 2017. *SEER Cancer Statistics Review, 1975-2014* [Online]. Bethesda, MD: National Cancer Institute. Available: https://seer.cancer.gov/csr/1975_2014/ [Accessed March 9, 2018].

International Atomic Energy Agency; Podgorsak, E. B. 2005. *Radiation oncology physics: A handbook for teachers and students*.

Ioannis, T., Per, N., Kiki, T., Elisabeth, K., Sven-Börje, E., Olof, J., Bengt, K. L., Constantin, K. & Panayiotis, M. 2007. NTCP modelling and pulmonary function tests evaluation for the prediction of radiation induced pneumonitis in non-small-cell lung cancer radiotherapy. *Physics in Medicine and Biology,* 52**,** 1055.

Jiang, Z., Earl, M. A., Zhang, G. W., Yu, C. X. & Shepard, D. M. 2005. An examination of the number of required apertures for step-and-shoot IMRT. *Physics in Medicine and Biology,* 50**,** 5653-63.

Kataria, T., Gupta, D., Bisht, S. S., Karthikeyan, N., Goyal, S., Pushpan, L., Abhishek, A., Govardhan, H. B., Kumar, V., Sharma, K., Jain, S., Basu, T. & Srivastava, A. 2014. Adaptive radiotherapy in lung cancer: dosimetric benefits and clinical outcome. *The British Journal of Radiology,* 87**,** 20130643.

Khan, F. M. 2014. *The Physics of Radiation Therapy,* Philadelphia, PA, Williams & Wilkins.

Kong, F.-M., Hayman, J. A., Griffith, K. A., Kalemkerian, G. P., Arenberg, D., Lyons, S., Turrisi, A., Lichter, A., Fraass, B., Eisbruch, A., Lawrence, T. S. & Ten Haken, R. K. 2006. Final toxicity results of a radiation-dose escalation study in patients with non-small-cell lung cancer (NSCLC): Predictors for radiation pneumonitis and fibrosis. *International Journal of Radiation Oncology*Biology*Physics,* 65**,** 1075-1086.

Kong, F.-M., Ten Haken, R. K., Schipper, M. J., Sullivan, M. A., Chen, M., Lopez, C., Kalemkerian, G. P. & Hayman, J. A. 2005. High-dose radiation improved local tumor control and overall survival in patients with inoperable/unresectable non–small-cell lung cancer: Long-term results of a radiation dose escalation study. *International Journal of Radiation Oncology*Biology*Physics,* 63**,** 324-333.

Krewski, D., Lubin, J. H., Zielinski, J. M., Alavanja, M., Catalan, V. S., Field, R. W., Klotz, J. B., Létourneau, E. G., Lynch, C. F., Lyon, J. I., Sandler, D. P., Schoenberg, J. B., Steck, D. J., Stolwijk, J. A., Weinberg, C. & Wilcox, H. B. 2005. Residential radon and risk of lung cancer: A combined analysis of 7 North American case-control studies. *Epidemiology,* 16**,** 137-145.

Kwint, M., Conijn, S., Schaake, E., Knegjens, J., Rossi, M., Remeijer, P., Sonke, J.-J. & Belderbos, J. 2014. Intra thoracic anatomical changes in lung cancer patients during the course of radiotherapy. *Radiotherapy and Oncology,* 113**,** 392-397.

Lee, C., Langen, K. M., Lu, W., Haimerl, J., Schnarr, E., Ruchala, K. J., Olivera, G. H., Meeks, S. L., Kupelian, P. A., Shellenberger, T. D. & Mañon, R. R. 2008. Assessment of parotid gland dose changes during head and neck cancer radiotherapy using daily megavoltage computed tomography and deformable image registration. *International Journal of Radiation Oncology*Biology*Physics,* 71**,** 1563-1571.

Lee, N., Puri, D. R., Blanco, A. I. & Chao, K. S. C. 2007. Intensity-modulated radiation therapy in head and neck cancers: An update. *Head and Neck,* 29**,** 387-400.

Li, J. G., Dempsey, J. F., Ding, L., Liu, C. & Palta, J. R. 2003. Validation of dynamic MLC-controller log files using a two-dimensional diode array. *Medical Physics,* 30**,** 799-805.

Li, Y., Sun, X., Wang, Q. I., Zhou, Q., Gu, B., Shi, G. & Jiang, D. 2015. A feedback constraint optimization method for intensity-modulated radiation therapy of nasopharyngeal carcinoma. *Oncology Letters,* 10**,** 2043-2050.

Lu, L. 2013. Dose calculation algorithms in external beam photon radiation therapy. *International Journal of Cancer Therapy and Oncology,* 1.

Ludlum, E. & Xia, P. 2008. Comparison of IMRT planning with two-step and one-step optimization: a way to simplify IMRT. *Physics in Medicine and Biology,* 53**,** 807-21.

Lyman, J. T. 1985. Complication probability as assessed from dose-volume histograms. *Radiation Research Supplement,* 8**,** S13-S19.

Ma, J., Zhang, J., Zhou, S., Hubbs, J. L., Foltz, R. J., Hollis, D. R., Light, K. L., Wong, T. Z., Kelsey, C. R. & Marks, L. B. 2008. The association between RT-induced changes in lung tissue density and global lung function. *International Journal of Radiation Oncology*Biology*Physics,* 72**,** S456.

Marks, L. B., Fan, M., Clough, R., Munley, M., Bentel, G., Coleman, R. E., Jaszczak, R., Hollis, D. & Anscher, M. 2000. Radiation-induced pulmonary injury: Symptomatic versus subclinical endpoints. *International Journal of Radiation Biology,* 76**,** 469-475.

Marks, L. B., Yorke, E. D., Jackson, A., Ten Haken, R. K., Constine, L. S., Eisbruch, A., Bentzen, S. M., Nam, J. & Deasy, J. O. 2010. Use of normal tissue complication probability models in the clinic. *International Journal of Radiation Oncology*Biology*Physics,* 76**,** S10-S19.

Martel, M. K., Ten Haken, R. K., Hazuka, M. B., Kessler, M. L., Strawderman, M., Turrisi, A. T., Lawrence, T. S., Fraass, B. A. & Lichter, A. S. 1999. Estimation of tumor control probability model parameters from 3-D dose distributions of non-small cell lung cancer patients. *Lung Cancer,* 24**,** 31-37.

Mavroidis, P., Plataniotis, G. A., Gorka, M. A. & Lind, B. K. 2006. Comments on 'Reconsidering the definition of a dose-volume histogram'--dose-mass histogram (DMH) versus dose-volume histogram (DVH) for predicting radiation-induced pneumonitis. *Physics in Medicine and Biology,* 51**,** L43-50.

Mayles, P., Nahum, A. & Rosenwald, J.-C. 2007. *Handbook of Radiotherapy Physics: Theory and Practice,* Boca Raton, FL, J. C. Taylor & Francis Group.

McNiven, A. L., Sharpe, M. B. & Purdie, T. G. 2010. A new metric for assessing IMRT modulation complexity and plan deliverability. *Medical Physics,* 37**,** 505-15.

Mihailidis, D. N., Plants, B., Farinash, L., Harmon, M., Whaley, L., Raja, P. & Tomara, P. 2010. Superiority of equivalent uniform dose (EUD)-based optimization for breast and chest wall. *Medical Dosimetry,* 35**,** 67-76.

Mihaylov, I. B. 2014. Mathematical formulation of energy minimization – based inverse optimization. *Frontiers in Oncology,* 4**,** 181.

Mihaylov, I. B. 2016. New approach in lung cancer radiotherapy offers better normal tissue sparing. *Radiotherapy and Oncology*.

Mihaylov, I. B., Lerma, F. A., Bzdusek, K., Penagaricano, J., Gardner, K., Ratanatharathorn, V. & Moros, E. G. 2009. Equivalent uniform dose inverse treatment planning for dynamic arc radiotherapy of prostate carcinoma. *International Journal of Radiation Oncology*Biology*Physics,* 75**,** S731-S732.

Mihaylov, I. B. & Moros, E. G. 2014. Mathematical formulation of DMH-based inverse optimization. *Frontiers in Oncology,* 4**,** 331.

Mihaylov, I. B. & Moros, E. G. 2015. Dose-mass inverse optimization for minimally-moving thoracic lesions. *Physics in Medicine and Biology,* 60**,** 3927-3937.

Mittauer, K., Lu, B., Yan, G., Kahler, D., Gopal, A., Amdur, R. & Liu, C. 2013. A study of IMRT planning parameters on planning efficiency, delivery efficiency, and plan quality. *Medical Physics,* 40**,** 061704.

Møller, D. S., Khalil, A. A., Knap, M. M. & Hoffmann, L. 2014. Adaptive radiotherapy of lung cancer patients with pleural effusion or atelectasis. *Radiotherapy and Oncology,* 110**,** 517-522.

National Cancer Institute. 2011. *Radon and Cancer* [Online]. Available: https://www.cancer.gov/about-cancer/causes-prevention/risk/substances/radon/radon-fact-sheet [Accessed March 9, 2018].

National Cancer Institute. 2017. *Head and Neck Cancers* [Online]. Available: https://www.cancer.gov/types/head-and-neck/head-neck-fact-sheet#q1 [Accessed March 10, 2018].

Niemierko, A. 1997. Reporting and analyzing dose distributions: A concept of equivalent uniform dose. *Medical Physics,* 24**,** 103-110.

Niemierko, A. 1999. A generalized concept of equivalent uniform dose (EUD). *Medical Physics,* 26.

Nioutsikou, E., Bedford, J. L., Christian, J. A., Brada, M. & Webb, S. 2004. Segmentation of IMRT plans for radical lung radiotherapy delivery with the step-and-shoot technique. *Medical Physics,* 31**,** 892-901.

Nioutsikou, E., Partridge, M., Bedford, J. L. & Webb, S. 2005a. Prediction of radiation-induced normal tissue complications in radiotherapy using functional image data. *Physics in Medicine and Biology,* 50**,** 1035-46.

Nioutsikou, E., Webb, S., Panakis, N., Bortfeld, T. & Oelfke, U. 2005b. Reconsidering the definition of a dose--volume histogram. *Physics in Medicine and Biology,* 50**,** L17.

Nutting, C., Dearnaley, D. P. & Webb, S. 2000. Intensity modulated radiation therapy: a clinical review. *The British Journal of Radiology,* 73**,** 459-469.

O'Daniel, J. C., Garden, A. S., Schwartz, D. L., Wang, H., Ang, K. K., Ahamad, A., Rosenthal, D. I., Morrison, W. H., Asper, J. A., Zhang, L., Tung, S.-M., Mohan, R. & Dong, L. 2007. Parotid gland dose in intensity-modulated radiotherapy for head and neck cancer: Is what you plan what you get? *International Journal of Radiation Oncology*Biology*Physics,* 69**,** 1290-1296.

Owen, D., Iqbal, F., Pollock, B. E., Link, M. J., Stien, K., Garces, Y. I., Brown, P. D. & Foote, R. L. 2015. Long-term follow-up of stereotactic radiosurgery for head and neck malignancies. *Head and Neck,* 37**,** 1557-1562.

Ricardi, U., Filippi, A. R., Guarneri, A., Giglioli, F. R., Ciammella, P., Franco, P., Mantovani, C., Borasio, P., Scagliotti, G. V. & Ragona, R. 2010. Stereotactic body radiation therapy for early stage non-small cell lung cancer: Results of a prospective trial. *Lung Cancer,* 68**,** 72-77.

Rodrigues, G., Lock, M., D'Souza, D., Yu, E. & Van Dyk, J. 2004. Prediction of radiation pneumonitis by dose–volume histogram parameters in lung cancer—a systematic review. *Radiotherapy and Oncology,* 71**,** 127-138.

Sanderson, R. J. & Ironside, J. A. D. 2002. Squamous cell carcinomas of the head and neck. *BMJ : British Medical Journal,* 325**,** 822-827.

Schmidt, M. L., Hoffmann, L., Kandi, M., Møller, D. S. & Poulsen, P. R. 2013. Dosimetric impact of respiratory motion, interfraction baseline shifts, and anatomical changes in radiotherapy of non-small cell lung cancer. *Acta Oncologica,* 52**,** 1490-1496.

Schwartz, D. L. & Dong, L. 2011. Adaptive radiation therapy for head and neck cancer--Can an old goal evolve into a new standard? *Journal of Oncology,* 2011.

Semenenko, V. A. & Li, X. A. 2008. Lyman–Kutcher–Burman NTCP model parameters for radiation pneumonitis and xerostomia based on combined analysis of published clinical data. *Physics in Medicine and Biology,* 53**,** 737.

Seppenwoolde, Y., Lebesque, J. V., de Jaeger, K., Belderbos, J. S. A., Boersma, L. J., Schilstra, C., Henning, G. T., Hayman, J. A., Martel, M. K. & Ten Haken, R. K. 2003. Comparing different NTCP models that predict the incidence of radiation pneumonitis. *International Journal of Radiation Oncology*Biology*Physics,* 55**,** 724-735.

Shepard, D. M., Earl, M. A., Li, X. A., Naqvi, S. & Yu, C. 2002. Direct aperture optimization: a turnkey solution for step-and-shoot IMRT. *Medical Physics,* 29**,** 1007-18.

Sher, D. J., Adelstein, D. J., Bajaj, G. K., Brizel, D. M., Cohen, E. E. W., Halthore, A., Harrison, L. B., Lu, C., Moeller, B. J., Quon, H., Rocco, J. W., Sturgis, E. M., Tishler, R. B., Trotti, A., Waldron, J. & Eisbruch, A. 2017. Radiation therapy for oropharyngeal squamous cell carcinoma: Executive summary of an ASTRO Evidence-Based Clinical Practice Guideline. *Practical Radiation Oncology,* 7**,** 246-253.

Siegel, R. L., Miller, K. D. & Jemal, A. 2018. Cancer statistics, 2018. *CA: A Cancer Journal for Clinicians,* 68**,** 7-30.

Verschakelen, J. A., Van fraeyenhoven, L., Laureys, G., Demedts, M. & Baert, A. L. 1993. Differences in CT density between dependent and nondependent portions of the lung: influence of lung volume. *American Journal of Roentgenology,* 161**,** 713-717.

Wang, J. Z., Mayr, N. A. & Yuh, W. T. C. 2008. Behind EUD. *Acta Oncologica,* 47**,** 971-972.

Wang, X. & Eisbruch, A. 2016. IMRT for head and neck cancer: reducing xerostomia and dysphagia. *Journal of Radiation Research,* 57**,** i69-i75.

Withers, H. R., Thames, H. D., Jr. & Peters, L. J. 1983. A new isoeffect curve for change in dose per fraction. *Radiotherapy and Oncology,* 1**,** 187-91.

Worthy, D. & Wu, Q. 2009. Parameter optimization in HN-IMRT for Elekta linacs. *Journal of Applied Clinical Medical Physics,* 10**,** 43-61.

Wu, Q., Chi, Y., Chen, P. Y., Krauss, D. J., Yan, D. & Martinez, A. 2009. Adaptive Replanning Strategies Accounting for Shrinkage in Head and Neck IMRT. *International Journal of Radiation Oncology*Biology*Physics,* 75**,** 924-932.

Wu, Q. & Mohan, R. 2000. Algorithms and functionality of an intensity modulated radiotherapy optimization system. *Medical Physics,* 27**,** 701-711.

Wu, Q., Mohan, R., Niemierko, A. & Schmidt-Ullrich, R. 2002. Optimization of intensity-modulated radiotherapy plans based on the equivalent uniform dose. *International Journal of Radiation Oncology*Biology*Physics,* 52**,** 224-235.

Yamada, K., Iwai, K., Kawamorita, R., Okuno, Y. & Nakajima, T. 2006. Change in dose distribution of three-dimensional conformal radiotherapy during treatment for lung tumor. *Radiation Medicine,* 24**,** 122-127.